CME THEORY AND MODELS

Report of Working Group D

T. G. FORBES[1,*], J. A. LINKER[2], J. CHEN[3], C. CID[4], J. KÓTA[5], M. A. LEE[2], G. MANN[6], Z. MIKIĆ[1], M. S. POTGIETER[7], J. M. SCHMIDT[8], G. L. SISCOE[9], R. VAINIO[10], S. K. ANTIOCHOS[3] and P. RILEY[2]

[1]*Institute for Earth, Oceans, and Space, University of New Hampshire, Durham, NH, USA*
[2]*Science Applications International Corp., San Diego, CA, USA*
[3]*Naval Research Laboratory, Washington, DC, USA*
[4]*Departamento de Física Universidad de Alcala, Alcala de Henares, Madrid, Spain*
[5]*Lunar and Planetary Laboratory, Department of Planetary Sciences, University of Arizona, Tucson, AZ, USA*
[6]*Astrophysikalisches Institut Potsdam, Potsdam, Germany*
[7]*Unit for Space Physics and School of Physics, North-West University, Potchefstroom, South Africa*
[8]*Imperial College, Space and Atmospheric Physics, The Blackett Lab., London, U.K.*
[9]*Boston University, Center for Space Physics, Boston, MA, USA*
[10]*Department of Physical Sciences, University of Helsinki, Helsinki, Finland*
*(*Author for correspondence: E-mail: terry.forbes@unh.edu)*

(Received 6 February 2006; Accepted in final form 6 April 2006)

Abstract. This chapter provides an overview of current efforts in the theory and modeling of CMEs. Five key areas are discussed: (1) CME initiation; (2) CME evolution and propagation; (3) the structure of interplanetary CMEs derived from flux rope modeling; (4) CME shock formation in the inner corona; and (5) particle acceleration and transport at CME driven shocks. In the section on CME initiation three contemporary models are highlighted. Two of these focus on how energy stored in the coronal magnetic field can be released violently to drive CMEs. The third model assumes that CMEs can be directly driven by currents from below the photosphere. CMEs evolve considerably as they expand from the magnetically dominated lower corona into the advectively dominated solar wind. The section on evolution and propagation presents two approaches to the problem. One is primarily analytical and focuses on the key physical processes involved. The other is primarily numerical and illustrates the complexity of possible interactions between the CME and the ambient medium. The section on flux rope fitting reviews the accuracy and reliability of various methods. The section on shock formation considers the effect of the rapid decrease in the magnetic field and plasma density with height. Finally, in the section on particle acceleration and transport, some recent developments in the theory of diffusive particle acceleration at CME shocks are discussed. These include efforts to combine self-consistently the process of particle acceleration in the vicinity of the shock with the subsequent escape and transport of particles to distant regions.

Keywords: Sun: Coronal Mass Ejections, CMEs, ICMEs, flares magnetic reconnection, shocks, solar energetic particles (SEPs)

Space Science Reviews (2006) 123: 251–302
DOI: 10.1007/s11214-006-9019-8

1. Introduction

T. G. FORBES, G. L. SISCOE

The life cycle of a CME encompasses a wide range of plasma processes in which the magnetic field plays a dominant role. Dynamo activity in the solar interior creates the magnetic field which builds up in the corona. Ultimately, this field erupts as a result of an instability or loss-of-equilibrium process which is yet to be identified. Once a CME is underway, a whole host of additional processes are triggered. These include magnetic reconnection, shock formation, and particle acceleration, among others. One of the main objectives of this chapter is to assess the current state of theoretical understanding of the various physical process involved in the life cycle of CMEs. Typically this understanding is brought about by using theoretical principles to construct mathematical models which describe both the form and evolution of CMEs as inferred from observations.

All models, whether numerical or analytical, require an initial state to be specified. For an MHD model, this means specifying eight variables (the three components of the magnetic field, the three components of velocity, density, and temperature) throughout the heliosphere prior to CME onset. Of these variables, the magnetic field components are the most critical. Because the magnetic field is inertially line-tied at the base of the corona (van der Linden *et al.*, 1994), only the magnetic field associated with coronal currents is available to drive CMEs. Unfortunately, this magnetic field is extremely difficult to measure. The best one can do at the present time is to estimate the field based on extrapolations of the vector fields at the photospheric and chromospheric levels. In practice, both measurement uncertainties and modeling limitations make it exceedingly difficult to deduce the pre-eruptive field solely from observations. Thus one is forced to make an initial guess for the pre-eruptive field and then evolve it in a manner consistent with the observed surface field to see if it leads to a CME-like eruption.

Because of the complexity of the equations which govern CME dynamics, much effort has been devoted in recent years to developing models using numerical methods (e.g. Mikić *et al.*, 1988; Biskamp and Welter, 1989; Forbes, 1990; Chen *et al.*, 2001; Gibson and Low, 1998; Antiochos *et al.*, 1999; Wu *et al.*, 2001; Amari *et al.*, 2000; Odstrcil *et al.*, 2002; Tokman and Bellan, 2002; Linker *et al.*, 2003; Roussev *et al.*, 2003, 2004; Kusano *et al.*, 2004). One of the hurdles that numerical models must cope with is the enormous range of spatial and temporal scales involved in the CME phenomenon, as shown in Figure 1. These scales range over 16 orders of magnitude from centimeters to hundreds of AU and from micro seconds to years. Considerable progress in covering this range has been made in the last few years by taking advantage of the fact that the flow of information in the solar wind, beyond the point where the fast mode Mach number exceeds one, is always outwards. This allows MHD codes to be chained together so that the output from one code is used as the input for another code. However, a large gap in coverage still exists between

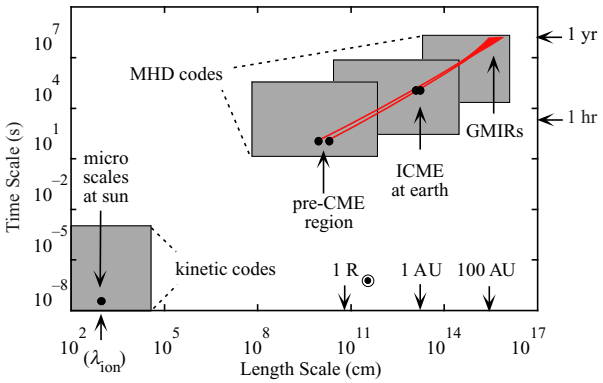

Figure 1. Time and length scales associated with CMEs as they propagate outwards through the solar system. The term "micro scales" refers to such parameters as the inertial length and gyro radius. The shaded rectangles indicate the ranges covered by existing numerical codes, and the curved lines indicate the leading and trailing edges of the CME as it progresses outwards through the solar system, first as a CME, then as an ICME (Interplanetary CME), and finally as part of a global merged interaction region (GMIR). Although the CME expands as it moves away from the Sun, it appears to contract in this log-log plot because it expands more slowly than the rate at which it moves away from the Sun.

the scale of the MHD codes and the kinetic codes required to model the physical processes occurring in current sheets (*i.e.*, reconnection) and shocks (*i.e.*, diffusive shock acceleration).

The heavy emphasis at the present time on the development of numerical models may lead to the impression that progress in modeling CMEs is just a matter of developing improved algorithms. While this may be true in some cases, it is not true for models of CME initiation, where the physical mechanism that triggers CMEs is unknown. Progress in this area depends on using both numerical and analytical models to develop a deeper understanding of the physical conditions that lead to an eruption. Although analytical models cannot cope with the same level of complexity as numerical models can, they are not restricted by resolution or scale limitations. Because analytical models provide a deeper level of insight into the underlying physics, they are often used in association with numerical models, either as a starting point or as an interpretive tool. An example of the former is the analytical model of Titov and Démoulin (1999), which has served as a starting point for the fully three-dimensional numerical simulations by Roussev *et al.* (2003, 2004) and Kliem *et al.* (2004).

Early models of CMEs developed in the 1970s were based on different principles than those used in present day models. Some of these early models, such as those of Steinolfson and Nakagawa (1977) and Dryer *et al.* (1979), assumed that CMEs are simply the result of a flare-generated blast wave. Today we know that, while some CMEs are flare associated, not all are. Furthermore, in many cases where there is a flare association, the CME can precede the flare (Wagner, 1981; Harrison, 1986).

Most importantly, the gas pressures generated during a flare are simply too small to blow open the magnetic field (Low, 1981; Emslie *et al.*, 2004).

While there is a general consensus that the energy that drives CMEs and flares originates from the coronal magnetic field, CME initiation has long been an area of substantial debate and continues to be so. Section 2 discusses three different models of CME initiation.

The dynamics of CMEs after initiation involves several factors. These include acceleration, expansion, drag, and distortion. Although acceleration and expansion are an integral part of the initiation process, they may also play a role in the long-term evolution of the CME either through a sustained operation of the forces which initiate the CME or through the interaction of the CME with the ambient solar wind. Drag and distortion result from the interaction of the CME with the ambient solar wind, corotating interaction regions (CIRs), and other CMEs. Section 3 explores our understanding of CME evolution and propagation through both analytical and numerical approaches.

A particularly important aspect of the evolution and propagation of CMEs are is the determination of the internal structure of ICMEs from in-situ measurements of the magnetic field. The strengths and limitations of these flux-rope fitting models are discussed in Section 4.

Large solar eruptions which generate high speed (1000–3000 km/sec) CMEs are the principal source of energetic particles produced in the solar system. A key aspect of the generation of solar energetic particle (SEP) events is the formation of shock waves, which is described in Section 5. SEP events can be subdivided into gradual and impulsive events. (The terms "gradual" and "impulsive" are used to refer to the evolution of the particle flux and do not refer to the X-ray profile of any associated flare.) Section 6 deals primarily with the theory of particle acceleration and transport of gradual events, as these are believed to be associated with CMEs.

2. CME Initiation

J. A. LINKER, T. G. FORBES, S. ANTIOCHOS, J. CHEN

Most CME initiation models today are based on the premise that CMEs and flares derive their energy from the coronal magnetic field. The currents that build up in the corona as a result of flux emergence and surface flows slowly evolve to a state where a stable equilibrium is no longer possible. Once this happens, the field erupts. If the eruption is sufficiently strong and the overlying fields not too constraining, plasma is ejected into interplanetary space. If strong magnetic fields exist in the erupted region, then bright, flare-like emissions occur. The latter is true, even if the field does not erupt (Švestka and Cliver, 1992).

At the present time, there is no consensus as to what the mechanism is that leads to the loss of a stable equilibrium. It may be purely ideal or involve non-ideal

processes like reconnection (Forbes, 2000; Low, 2001). The possibility also remains that very slow (<150 km/s) CMEs which undergo weak acceleration over a period lasting as long as a day (Sirivastava *et al.*, 2000; Zhang *et al.*, 2004) may not involve a release of stored magnetic energy at all. For these CMEs the observed rates of flux emergence in the photosphere is of the same order as that required by the flux injection model (Krall *et al.*, 2000). Unlike most CME models, this model does not involve the storage of magnetic energy in the corona prior to onset. Instead, it injects magnetic flux and energy into the corona during the eruption.

One of the difficulties that all storage models face is explaining how it is possible to decrease the magnetic energy in the corona even though the ejection of the CME stretches the magnetic field as it moves outwards into interplanetary space. The stretching of the field creates an apparent paradox, since it implies that the magnetic energy of the system is increasing, whereas storage models require it to decrease. Aly (1984, 1991) and Sturrock (1991) have argued that for a simply-connected field, the fully-opened field-configuration always has a higher magnetic energy than the corresponding force-free field. This constraint seems to imply that storage models are energetically impossible (see Mikić and Lee, 2006, this volume). However, there are several possible ways around it. First, the magnetic field may not be simply connected and contain knotted field lines. Second, it may contain field lines that are completely disconnected from the surface. Third, an ideal-MHD eruption can still extend field lines as long as it does not open them all the way to infinity. Fourth, an ideal-MHD eruption may be possible if it only opens a portion of the closed field lines. Fifth, small deviations from a perfectly force-free initial state might make a difference. And finally, a non-ideal process, specifically magnetic reconnection, invalidates the constraint.

In the following subsections we describe three examples of CME initiation models. See Mikić and Lee (2006) in this volume for a discussion of the similarities and differences in the underlying physics of these models.

2.1. Flux Rope Models and Flux Cancellation

Coronal mass ejections are frequently associated with prominence eruptions as well as solar flares. Prominences (called filaments when observed on the solar disk) support cool, dense chromospheric material ($\sim 10^4$ K and $10^{10}-10^{11}$ cm^{-3}) against solar gravity in the surrounding hot, tenuous corona ($\sim 10^6$ K and 10^7-10^9 cm^{-3}). They are observed to lie above magnetic neutral lines in the photosphere and near the base of helmet streamers (regions of closed magnetic field that have confined the coronal plasma). The magnetic field in the prominence often exhibits "inverse polarity," meaning that when the coronal magnetic fields embedded in the prominence cross over the neutral line, they point in the direction opposite to that indicated by the photospheric magnetic field polarity (Leroy *et al.*, 1983, 1984). The prominence magnetic field is itself nearly aligned with the filament channel (Martin *et al.*, 1994;

Martin and Echols, 1994), indicating a highly sheared (and therefore magnetically energized) configuration.

The idea that a flux rope could explain the inverse polarity of a prominence dates back to the Kuperus and Raadu (1974) prominence model. In that model, a current filament (in two dimensions) produces closed magnetic loops that can support prominence material above the photosphere. Since that time there have been a number of authors who have focused on the support of prominence material by helical field lines and/or the disruption of these configurations as the possible cause of prominence eruptions and coronal mass ejections (van Ballegooijen and Martens, 1989; Forbes and Isenberg, 1991; Lin *et al.*, 1998; Titov and Démoulin, 1999; Amari *et al.*, 2000; Linker *et al.*, 2001; Low, 2001; Sturrock *et al.*, 2001; Low and Zhang, 2002; Amari *et al.*, 2003a,b; Birn *et al.*, 2003; Linker *et al.*, 2003; Roussev *et al.*, 2003, 2004; Kliem *et al.*, 2004).

Two possibilities exist for the formation of the flux rope. The flux rope could emerge intact from below the photosphere (Rust and Kumar, 1994; Lites *et al.*, 1995; Fan, 2005) or be formed as the result of motions at the photosphere or above. In this review, we focus on the second possibility, that flux ropes are first formed, and subsequently erupt, as a result of flux cancellation at the photosphere (defined below). Once a flux rope structure has formed in the corona, the susceptibility of the structure to eruption shouldn't depend on its origin.

2.1.1. *What is Magnetic Flux Cancellation?*

Martin *et al.* (1985) defined flux cancellation observationally as the mutual disappearance of magnetic fields of opposite polarity at the neutral line separating them. Martin *et al.* (1985) chose the term "flux cancellation" carefully, so as not to convey any theoretical interpretation of the process; they recognized that flux elements might be submerging, annihilating, or being expelled upward. Flux cancellation occurs everywhere on the Sun, (Livi *et al.*, 1985); observations have shown it to be active at filament sites (Litvinenko and Martin,, 1999; Wang, 2001) and in active regions as they disperse (Martin *et al.*, 1985). During this time, filaments are frequently observed to form along the neutral line. At times, these filaments disappear, presumably due to eruption, and may even reform in the same location later. This dispersal of magnetic flux is thought to occur on a small spatial scale by annihilation and submergence of magnetic dipole elements and has been modeled as a convective-diffusive process on a large scale (Wang *et al.*, 1989; Wang and Sheeley, 1990).

Associations of flux cancellation with solar flares have been noted previously (Livi *et al.*, 1989). More recently, flux cancellation has been associated with CMEs (Lin *et al.*, 2004). A particularly striking example is the "Bastille Day" event, an X5.7 flare and associated fast CME that occurred in an active region (NOAA AR 9077) on July 14, 2000. Flux cancellation was observed throughout this event

(Kosovichev and Zharkova, 2001) and has been interpreted as the cause of the massive eruption (Somov *et al.*, 2002).

2.1.2. *Flux Cancellation: Theoretical Interpretation*

The recognition that flux cancellation is active at filament sites and during the eruptive process led to the interpretation that the cancellation was in fact the annihilation of magnetic flux at the photosphere through reconnection. Using this interpretation, van Ballegooijen and Martens (1989) investigated the consequences of flux cancellation at the neutral line of a 2.5D sheared arcade configuration. They computed sequences of force-free equilibria to show that flux cancellation leads to the formation of a flux rope. The helical field lines of the model flux rope contained dips capable of supporting prominence material, and the rise in the equilibrium height of the flux rope with increased flux cancellation suggested possible eruptive behavior.

Calculations by Forbes and Isenberg (1991), Forbes *et al.* (1994) and Lin *et al.* (1998) investigated the stability of flux ropes embedded in a background field. They found that that once a flux rope is formed, continuation of the flux cancellation process can result in a loss of equilibrium. The new lower-energy equilibrium contains a current sheet and a higher height for the flux rope. While the energy release in this ideal process is relatively small, the new equilibrium height of the flux rope can be many solar radii from the Sun. The reason for this transition in equilibria can be understood as follows: The magnetic pressure forces in the flux rope want the rope to expand; these forces are restrained by tension in the surrounding fields. Flux cancellation converts the restraining field into magnetic flux in the rope, increasing the magnetic pressure. Eventually the system reaches a point that no nearby equilibrium is accessible (see Figure 2). In reality, the new equilibrium with a flux rope high above the photosphere is untenable; the flux rope would be pulled outward by the solar wind. Significant magnetic energy release could then occur through magnetic reconnection at the current sheet. Exploring this aspect of the problem is intractable analytically and must be studied with numerical simulations.

2.1.3. *Flux Cancellation: MHD Computations*

Amari *et al.* (2000) investigated the formation and eruption of a magnetic flux rope by flux cancellation in localized 3D Cartesian geometry. These calculations neglected the plasma pressure and were thus an appropriate approximation for an active region at heights low in the corona. They showed the formation and subsequent eruption of a flux rope when a sheared arcade was subjected to flux cancellation. Amari *et al.* (2003a,b) studied further examples of eruptions in this geometry and showed that the flux cancellation process causes little change to helicity of the sheared configuration.

Linker *et al.* (2003) performed numerical calculations that appear to have a close correspondence to the theoretical work of Lin *et al.* (1998). These calculations

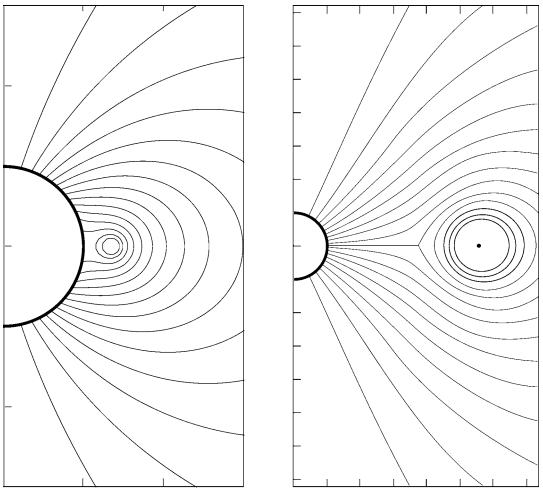

Figure 2. Azimuthally-symmetric flux rope model showing the ideal MHD transition from a flux rope in equilibrium close to the Sun (a) and the same flux rope at a large distance from the Sun after the transition (b). A current sheet forms as a result of this transition (after Lin *et al.*, 1998).

solved the full MHD equations and included the important effect of the solar wind. First, a helmet streamer configuration is developed by combining a spherically symmetric solar wind solution with a potential magnetic field and integrating the MHD equations in time until the solution settles down to an equilibrium. A helmet streamer with closed field lines forms, surrounded by open field lines along which the solar wind flows outward. To provide a source of free magnetic energy for the eruption, a shear flow is introduced near the neutral line of the streamer. This shear flow is not intended to model actual flows on the Sun. It is just a convenient mechanism for producing strongly sheared field lines that are nearly aligned with the neutral line, a frequently observed characteristic of filaments (Martin *et al.*, 1994). Figure 3 at $t = 1300\tau_A$ (τ_A, the Alfvén time, is 12 minutes), shows projected magnetic field lines and current density for the sheared helmet streamer. The investigation of the effect of flux cancellation begins at this point in the calculation. The change in flux is applied by specifying the tangential component of the electric field at the boundary, $\mathbf{E}_{t0}$. For example, when $\mathbf{E}_{t0} = 0$, B_{r0} (the radial magnetic field at the solar boundary) remains fixed in time. In order to specify a desired change in the magnetic flux, a nonzero $\mathbf{E}_{t0}$ is specified. This electric field drives converging flows and reduces the flux at the neutral line, as is believed to occur in the flux cancellation process (van Ballegooijen and Martens, 1989).

Flux cancellation first forms a stable flux rope configuration within the helmet streamer (Figure 3, $t = 1350\tau_A$). Without further flux cancellation or other imposed changes to the configuration, the flux rope will remain stable indefinitely. Therefore,

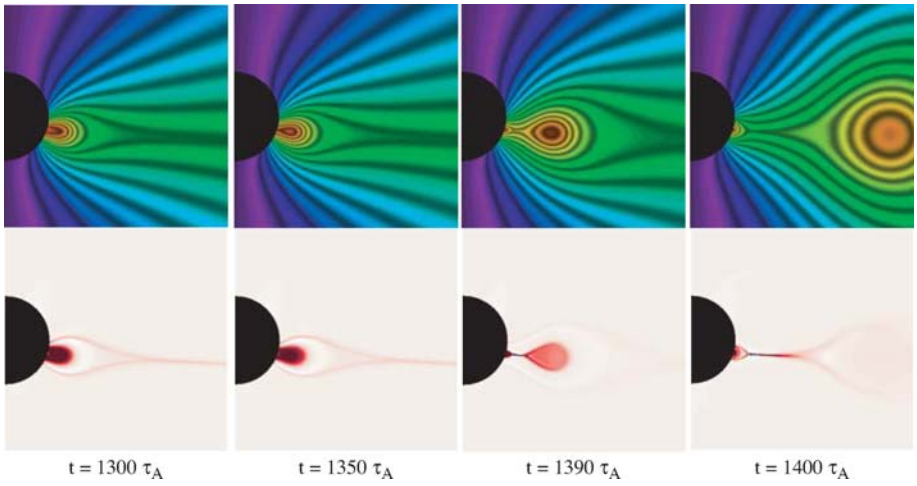

Figure 3. MHD Simulation of a helmet streamer eruption triggered by flux cancellation (after Linker *et al.*, 2003). The stripes in the top panels show projected field lines (there is also a B_ϕ component of the magnetic field out of the plane). The bottom panels shows the current density J_ϕ out of the plane. Time in Alfvén scale times ($\tau_A = 12$ minutes) is indicated. Note the similarity of the flux rope eruption and current sheet formation to that shown in Figure 2.

on the real Sun, prominences could form by this mechanism and remain stable for many days or weeks. Lionello *et al.* (2002) and van Ballegooijen (2004) have studied flux rope formation via this mechanism for more realistic field configurations. With continued flux cancellation, the helmet streamer is destabilized, subsequently erupting into the outer corona as shown in the last two frames of Figure 3. The eruption of the flux rope and the formation of the current sheet is reminiscent of the ideal calculation by Lin *et al.* (1998). However, for the resistive MHD calculation, energy is released rapidly through reconnection at this sheet. Linker *et al.* (2003) found that about 1.75×10^{32} ergs of magnetic energy was released, with about 1/2 of the energy going into kinetic energy.

Figure 4 shows the same eruptive process for a 3D simulation (flux cancellation begins at t_0 in the calculation). In this case the same helmet streamer configuration is used, but flux is reduced only along one side of the Sun. In the 3D eruption, the ends of the flux rope are attached to the photosphere. The polarization brightness is shown in the topmost panels. The images show, albeit in a very idealized way, the three part structure often seen in CMEs (Illing and Hundhausen, 1985). Roussev *et al.* (2004) have also demonstrated a flux-cancellation initiated eruption for a more realistic 3D configuration; they used low-resolution synoptic maps as the basis for their configuration.

2.1.4. *Discussion and Future Developments*

The flux cancellation mechanism is an attractive hypothesis for explaining both prominence formation and the initiation of CMEs with associated prominence

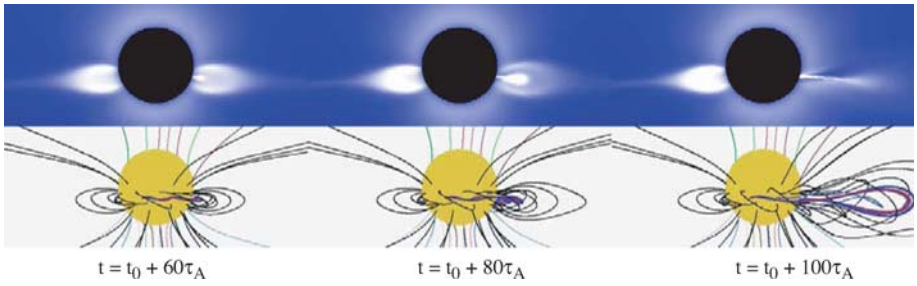

Figure 4. Polarization brightness (that would be observed by a coronagraph if this were a real CME) and magnetic field lines for an MHD simulation of a 3D eruption (see text). The black (yellow) disk in the top (bottom) frames shows the position of the Sun. The viewpoint is slightly above the equator, so the current sheet is not viewed edge on. Black and multi-colored field lines show the helmet streamer and open field lines. At $t = t_0$, flux cancellation begins; flux is canceled only on one hemisphere of the Sun. The blue and red field lines show the flux rope. The eruption in 3D is very similar to the 2D case, although the flux rope field lines are now line-tied to the Sun. (After Linker *et al.*, 2003.)

eruptions. The mechanism assumes that the frequent cancellation events that occur during the lifetime of an active region annihilate some of the surface magnetic flux and convert sheared fields in the active region into a flux rope. The flux rope, which supports the cool, dense material observed in prominences, can be stable for hours, days or weeks until cancellation increases the magnetic pressure in the flux rope to the point that it exceeds the surrounding tension, causing the violent eruption. The simulation results by Linker *et al.* (2003) indicate that the magnetic fields associated with the initial filament are a small fraction of the volume of the flux ropes observed in interplanetary space by in-situ spacecraft. This is because the resulting eruption ejects a portion of the overlying streamer belt. The flux cancellation mechanism avoids any problems with the Aly-Sturrock energy limit. The ideal process identified by Lin *et al.* (1998) does not violate the limit (the fields always remain closed); the reconnection that rapidly releases energy (Linker *et al.*, 2003) is a non-ideal process not accounted for by the theorem.

While the mechanism is certainly plausible, it is at this point far from being predictive. The amount of cancellation required to cross the threshold for eruption depends strongly on the details of the magnetic configuration, which are not easily deduced from presently available solar observations. To verify or rule out this mechanism, calculations need to be performed that start from a detailed model of an observed active region. Then one needs to study whether observed motions and flux changes can trigger an eruption. It is also important for analytic formulations of the mechanism to provide more insights into the loss of equilibrium process in 3D, particularly when line-tying is present. Modeling of the emergence of fields through the photosphere can help to clarify what subphotospheric processes occur that lead to the phenomena that we observe as flux cancellation.

When more detailed computations are available, new observations will undoubtedly be crucial for progress. Detailed sequences of vector magnetograms in filament

channels and active regions, coupled with high-resolution X-ray and EUV imaging, can help to substantiate (or not) theoretical and computational models of the flux cancellation mechanism. Future missions such as *Solar-B*, STEREO, and SDO, as well as ground-based observations from SOLIS will provide these measurements. The confluence of more sophisticated models and improved observational capabilities over the next few years will likely provide the opportunity to verify or invalidate the role of flux cancellation as a trigger for CMEs.

2.2. The Breakout Model

2.2.1. *Physical Mechanism*

As discussed above, the most widely accepted models for CME/eruptive flares are those in which the energy for the eruption is stored in coronal magnetic fields, specifically, the strongly sheared/twisted field of a filament channel (see reviews by Forbes (2000), Klimchuk (2001), Low (2001), Wu *et al.* (2001) and Lin *et al.* (2003)). The basic picture is that a CME represents the catastrophic disruption of the force balance between the upward magnetic pressure of the highly-sheared filament-channel field and the downward tension of overlying quasi-potential field. Since the upward pressure force is constrained to increase only slowly, either by flux emergence or by photospheric motions, explosive eruption must be due to the fast decrease of the downward tension.

Three general types of reconnection models for CME initiation have been proposed, differing primarily in magnetic topology and in location of the reconnection. In this section we focus on the so-called breakout model, in which reconnection is postulated to occur external to the filament channel, between the quasi-potential overlying flux and neighboring flux systems (Antiochos *et al.*, 1999; Antiochos and DeVore, 1999). Consequently, an essential requirement for the breakout model is that the coronal magnetic topology is due to a multipolar flux distribution at the photosphere and that it contains at least one null point where reconnection can occur.

The basic mechanism is shown in Figure 5, which presents results from recent 2.5D (axisymmetric, with two spatial dimensions and three components of the vector fields) simulations by MacNeice *et al.* (2004). The initial field (first panel) is potential and contains four flux systems, with a coronal null "point" (latitudinal circle, in 2.5D). The photospheric flux distribution consists of four polarity regions separated by three neutral lines. For clarity, only field lines originating in the northern hemisphere are shown in the figure, but the system is symmetric about the equator. In order to produce an eruption, a filament channel must be added to this potential field. Observations suggest that the Sun creates filament channels through some not-yet understood process involving flux emergence, cancellation, and/or post-emergence subsurface motions (Martin *et al.*, 1984, 1994). In this simulation, the filament channel was created by simply imposing a slow, photospheric shear-flow localized at the equatorial neutral line. In fact, recent theoretical and observational (Welsch *et al.*, 2004) results appear to support such a flow. Furthermore,

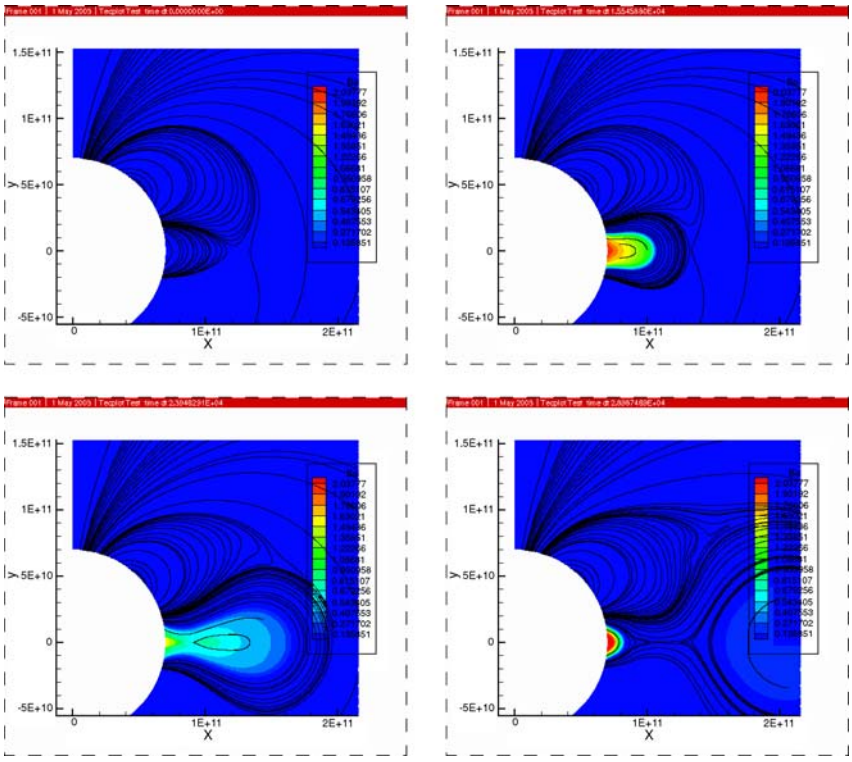

Figure 5. Selected field lines at four times during an axisymmetric simulation of the breakout model. The four panels correspond to times $t = 0$, 4.3, 6.6, and 8.1 hours. Also plotted are contours of B_ϕ, which show the location and magnitude of the applied shear.

the breakout model is expected to be insensitive to the details of the filament channel formation process. Unlike most other models, which require a particular form for the photospheric evolution and the filament field in order to obtain eruption, breakout should work for either flux emergence or cancellation and either a sheared arcade or a twisted flux rope.

The effect of the photospheric shear flow is to generate a large magnetic component parallel to the neutral line, (B_ϕ), which produces an upward magnetic pressure (second panel). This added pressure causes the overlying potential field lines to expand outward and increase their net downward tension, leading to the basic pre-eruption force balance described above. Another effect of the outward expansion is to stretch radially the field near the null so that the null region deforms into a current sheet structure (second and third panels of Figure 5). As long as the width of the current sheet is large compared to the grid scale of the simulation, the effective diffusion is negligible, and the system maintains a true stable equilibrium. It should be emphasized that such a stable energy buildup phase is necessary for all explosive eruption models.

As the shearing continues, however, the width of the current sheet structure at the null eventually decreases to the grid scale, and reconnection begins. Once reconnection appears, the outward expansion rate grows exponentially, even with no further shearing, because reconnection removes the overlying flux, thereby decreasing the downward tension. The tension decrease allows the sheared field to expand outward faster, which, in turn, drives faster reconnection. Energetically, the breakout mechanism can be considered to yield explosive eruption by minimizing the amount of flux that must open along with the sheared filament channel field.

For this simulation, the trigger for the eruption is the turn-on of numerical resistivity due to its grid dependence. It is likely that a scale-dependent resistivity due to collisionless effects or current-driven instabilities also operates in the Sun's corona. The important point for the model, however, is not that the breakout reconnection has a rapid turn-on, but that once it is on, the subsequent global evolution of the system causes the current sheet width to decrease and to drive the reconnection at an ever-faster rate.

One consequence of the eruption is that originally low-lying field lines become so expanded radially that they begin to approach the open state and, consequently, a vertical current sheet forms deep inside the sheared field region leading to reconnection there (last panel of Figure 2.1). It should be emphasized that this reconnection is completely distinct from the breakout reconnection ahead of the eruption. The reconnection that begins deep inside the erupting field corresponds to the usual flare reconnection and is common to nearly all CME models. In the breakout model, the flare reconnection does not initiate the eruption, but it may help accelerate it. Furthermore, the twisted flux rope that forms due to this flare reconnection (last panel) is a consequence of eruption, not its cause.

2.2.2. *Relation to Observations*

The major distinguishing predictions of the model are the breakout reconnection itself and the required multipolarity of the pre-eruption topology. A number of recent studies have identified observed CMEs/eruptive-filament events that appear to be explained by the breakout model (Aulanier *et al.*, 2000; Sterling and Moore, 2001, 2004; Sterling *et al.*, 2001; Wang *et al.*, 2003; Manoharan and Kundu, 2003; Subramanian *et al.*, 2003; Gary and Moore, 2004), but these studies are mainly qualitative in nature. They present evidence for particle acceleration, or for heating attributed to reconnection that is far removed from the flare ribbons, and/or for a multipolar magnetic topology in the corona. Perhaps the best example is that of Aulanier *et al.* (2000), who present compelling evidence for reconnection at a coronal null point prior to and during the July 14, 1998 flare. There has also been some quantitative analysis of the 2.5D simulation results for comparison with generic coronagraph and in-situ observations. Lynch *et al.* (2004) find that the breakout model reproduces the three-part structure commonly seen in coronagraph images, and the linear force-free flux rope magnetic structure that is often measured in ICMEs at 1 AU. At present, however, it is fair to state that there has not been a

rigorous quantitative test of the model against a real event. The reasons are that all actual events are fully 3D and generally have a complex topology. Only now are 3D simulations of breakout being undertaken, and only for idealized topologies.

Although a definitive, quantitative comparison between the breakout model and data is not yet available, there are several aspects of the model that make it unique in being able to explain the observations. First, it has long been known that solar eruptions occur predominately in magnetically complex regions. In fact, the magnetic complexity of an active region is often used as a predictor of whether it will produce major flares. The breakout model naturally explains why complexity leads to eruption. Second, it is also well known that eruptions can occur under all kinds of photospheric conditions, from strong active regions to very quiet high-latitude filaments, and during flux emergence, or flux cancellation, or during periods of apparently fixed flux. Unlike other models which require a particular form for the photospheric evolution, the breakout mechanism requires only that the filament channel builds up free energy and, hence, the model is compatible with a wide range of observed photospheric conditions. Finally, the height at which the eruption begins exhibits a great deal of variability. In some events the eruption extends far down into the chromosphere (as determined by the locations of the flare ribbons), but in others only the corona well above a visible filament/prominence erupts. Again it is difficult to reconcile these observations with many of the models; but since breakout places no special requirement on the filament channel field, it is completely flexible as to how much of the field erupts in any one event.

On the other hand, it should be emphasized that the model has no flexibility with respect to magnetic complexity. Breakout cannot operate in a truly bipolar field. Furthermore, even if the field is complex, breakout requires the occurrence of external reconnection that transfers a substantial amount of flux from the overlying erupting filament channel. It is far from evident that such a flux transfer is present in all eruptions.

2.2.3. *Future Developments*

The necessary developments of the model are straightforward. First, the model must be extended to fully 3D topologies. Some success has already been demonstrated in 3D (Antiochos and DeVore, 1999), but this was for a topology containing a separator line in the corona and unlikely to be common on the real Sun. The extension of the 2.5D axisymmetric spherical models to a fully 3D geometry is clearly required. Furthermore, this type of work needs to be performed by more than one group, because the results of complex 3D simulations require verification by multiple codes.

Second, the sensitivity of the model to the assumed form for the resistivity needs to be determined. As discussed above, the resistivity must have a switch-on nature so that the breakout reconnection does not start too early and so that once the eruption is underway, the reconnection can keep pace. All the simulations

to date have been performed with numerical resistivity, which has a strong scale dependence. Calculations need to be undertaken with different resistivity models and with different values for the resistivity in order to confirm that the model can yield fast eruptions even for large magnetic Reynolds number. Some of this work has already been performed in 2.5D (MacNeice *et al.*, 2004), but the 3D case is completely unexplored.

If these two developments are successful, the next step would be to test the model against real solar events by using observed photospheric magnetic and velocity fields as input and comparing the resulting eruption with coronal observations. Of course, these will be challenging simulations even with an adaptive mesh refinement code; but the codes and the hardware are now in hand. We expect that the next few years will prove to be decisive for determining the validity of not only the breakout model but all the present models for CME initiation.

2.3. Flux Injection Model

The theoretical model of Chen (1989, 1996) hypothesizes that the underlying magnetic field of a CME is that of a three-dimensional magnetic flux rope. The initial flux rope is assumed to be in MHD equilibrium, and the eruption occurs in response to the "injection" of poloidal magnetic flux Φ_p into the flux rope. The model then uses an approximate form of the MHD equations to calculate the evolution of the flux rope. No explicit prescription of the magnetic field is provided by this model, although it does include the effects of inertial line-tying at the solar surface. It also assumes that reconnection occurs so readily that any current sheets which form during the evolution have a negligible effect on the dynamics of the flux rope.

Since the launch of SOHO, the model has been extensively tested against EIT and LASCO data. It was shown by direct comparisons with data that the model solutions closely match the observed height-time profiles of CMEs within the LASCO field of view (Chen *et al.*, 1997, 2000; Wood *et al.*, 1999; Krall *et al.*, 2001). In particular, by analyzing the dynamics and morphology of 11 LASCO CMEs Krall *et al.* (2001) showed that flux-rope CMEs constitute a significant identifiable class. A prediction of the model is that the aspect ratio of a CME, defined as the ratio of the leading-edge height and the transverse width, is nearly constant except during the initial acceleration phase. This constancy of the height-to-width ratio at large distances from the sun is a general property of flux rope models, and it follows from the conservation of magnetic flux (Kumar and Rust, 1996). Significantly, this property, representing the dynamics in two orthogonal directions, was verified in these LASCO CMEs. In addition, synthetic coronagraph images (Chen *et al.*, 2000) show that the 2-D projections of 3-D flux ropes exhibit the generic morphological features of the prototypical 3-part CMEs (Illing and Hundhausen, 1986). It was also found that a model CME evolves into an interplanetary

flux rope that resembles observed magnetic clouds at 1 AU and beyond (Chen, 1996).

The above studies show that the flux rope hypothesis is quantitatively consistent with observed CMEs. However, the coronal magnetic field is not directly measurable at this time. Thus, our understanding of magnetic structure, which is based on the morphology of projected density features, depends on various assumptions. The existing CME models assume as initial structures either magnetic arcades (*e.g.*, Forbes and Priest, 1995; Linker and Mikić, 1995; Antiochos *et al.*, 1999; Chen and Shibata 2000; Cheng *et al.*, 2003) or flux ropes (*e.g.*, Chen, 1989, 1996; Wu *et al.*, 1999; Amari *et al.*, 2000; Roussev *et al.*, 2003, 2004). Both model constructs lead to flux ropes after the eruption. In the former scenario, the initial arcade evolves into a flux rope via macroscopic reconnection. The key question is at what stage of the eruption the flux rope is formed. In this respect, Chen and Krall (2003) showed that if the initial structure is a flux rope or becomes a flux rope before the main acceleration phase, the acceleration peaks at a critical height Z_* given by $Z_* = S_f/2$, where Z refers to the height of the centroid of the apex from the solar surface and S_f is the distance between the two stationary footpoints at the base of the corona. This scaling law is universal in that it depends only on the 3-D toroidal flux rope geometry with constant S_f regardless of the speed of eruption. For typical CMEs, S_f is of the order of 1/2–1 R_s so that the acceleration maximum occurs below 2–3 R_s, while CMEs associated with polar crown prominence having maximum acceleration in the 3–4 R_s height range. This was shown to be true for a number of CMEs well-observed by LASCO, implying that the initial structures underlying these CMEs were flux ropes before the onset of the main acceleration phase. The theoretical result is also supported by an MHD simulation of a toroidal flux rope with fixed footpoints (Roussev *et al.*, 2003, 2004).

The basic physics embodied in the theory of Chen (1989) is that the flux rope motion is determined by the Lorentz force, pressure gradient, drag on the ambient coronal plasma, and gravity. The main driver is a specific form of Lorentz force, the so-called hoop force acting on curved current-carrying plasma (Shafranov, 1966; Anzer, 1978). This force is proportional to κ^2, where $\kappa = 1/R$ is the major radial curvature. The initial flux rope is set into motion by increasing the poloidal flux Φ_p of the system. In the model of Chen (1989, 1996), this is interpreted as injection of magnetic energy from subphotospheric sources ultimately determined by the solar dynamo at the base of the convection zone. However, the model by itself does not require a subphotospheric source. It is equally possible to interpret the mathematical function $\Phi_p(t)$ as derived from magnetic energy stored in the corona. For example, if the initial structure is an arcade that evolves into a flux rope via reconnection, a flux rope is created in this process so that its poloidal flux Φ_p increases from zero, or some initial value, to the final value when the flux rope is fully formed. In such a model, the increase in the function $\Phi_p(t)$ can be interpreted as energy injected into the flux rope via macroscopic reconnection. The ensuing

flux motion is determined by how the flux rope is formed, *i.e.*, by the reconnection process.

3. CME Evolution and Propagation

J. SCHMIDT, G. L SISCOE

3.1. CME DYNAMICS

3.1.1. *Statement of Problem*

After an abrupt formation in the solar corona, a CME propagates into and through the interplanetary medium as an ICME, and then by assimilation into merged interaction regions in the outer heliosphere loses its identity. To describe this process quantitatively defines the CME-propagation problem, which is the subject of this section. Two approaches have been pursued, analytical formulation and MHD simulation. In the analytical approach the problem is to specify the equations that describe the motion through the spatially varying solar wind of a compressible (ICME) body subject to acceleration, deceleration, and deformation forces. Ordinary differential equations determine the position of the ICME and its geometry as a function of time. In MHD simulations, by contrast, the motion field and the force field are specified at every point of a simulation grid (and not at the center of mass of an ICME as in the analytic formulation), which requires partial differential equations (actually finite-difference representations of them). A CME and its interplanetary trajectory can be traced by following a closed contour of a scalar field such as normalized density.

This section focuses mainly on the analytical approach because, unlike simulations, it treats a CME as a distinct object and, thus, it explicitly describes the forces that propel, expand, and deform the object. We use a parameterized equation of motion that captures a CME's rapid acceleration from rest followed by slow deceleration. Comparing the results of different choices of parameters against observations favors some choices over others. The choices entail specifying the initial parameters of the CME, the nature of the force that propels a CME from the Sun, the nature of the drag force that couples it to the solar wind, and the aspect of "virtual mass" (explained below). We begin by reviewing selected observations that bear on discriminating between choices and end by comparing results of the analytical approach against those of an MHD simulation.

3.1.2. *Observations to Test Models*

The relevant observations are the initial acceleration of CMEs near the Sun, the subsequent acceleration or deceleration between the Sun and Earth, the size and rate of expansion of the ICME at 1 AU, the shape of the cross section of the ICME at 1 AU, and the typical values of the magnetic field strength and mass density within the ICME at 1 AU. Regarding CME acceleration near the Sun, in a statistical analysis

of 24 CMEs, Zhang (2005) found typical values for acceleration and duration of acceleration to be respectively 200 m/s^2 and 40 min. These numbers give 0.82 Rs as a typical acceleration distance, whereupon the CME has reached a speed of 480 km/s. But the range in these numbers between events was considerable; for example, the acceleration ranged from a few m/s^2 to nearly 1000 m/s^2.

In a separate analysis of 28 CMEs, Gopalswamy *et al.* (2000) found speeds of CMEs near the Sun ranging from 124 km/s and 1,056 km/s. In other cases, speeds as high as 2500 km/s have been observed (Gopalswamy, private communication, 2004). These speeds were derived by measuring the plane-of-the-sky speed of the fastest CME feature as seen by the LASCO coronagraphs. Thus, these speed values may differ substantially from the radial CME speed, depending upon which way the CME was headed (see the discussion in Schwenn *et al.*, 2006, this volume). This uncertainty, however, does not detract from using the speeds to illustrate model forces. Between the Sun and Earth, fast CMEs decelerate and slow CMEs accelerate so that they arrive at 1 AU with speeds closer to that of the ambient solar wind. The same Gopalswamy *et al.* (2000) analysis correlated plane-of-the-sky CME speeds (u) as measured in coronagraph images with the speed of the resulting ICME at 1 AU to derive the following empirical formula for their in-transit acceleration a (deceleration being negative acceleration)

$$a[\mathrm{m/s^2}] = 1.41 - 0.0035\,u[\mathrm{km/s}] \tag{1}$$

We will refer to velocity-versus-distance profiles based on this formula as the Gopalswamy *et al.*, template against which we will compare predictions of the equation of motion to be discussed in the next section. (See Section 3.2 of Forsyth *et al.*, 2006, this volume, for more discussion of CME speeds.)

Support for the validity of the Gopalswamy *et al.*, template comes from Reiner *et al.* (2003), who used simultaneous radio and white light observations to document the deceleration of fast CMEs between the Sun and Earth. Their observations are consistent with a constant deceleration (such as is assumed in the construction of the Gopalswamy *et al.*, template) and inconsistent with a deceleration that decreases with distance from the Sun (a result that in the next section we shall use as a discriminator between model options).

The next observational discriminator listed above is the size and expansion speed of an ICME at 1 AU. The radial (from the Sun) dimension of an ICME at 1 AU is typically 0.2 to 0.25 AU (Klein and Burlaga, 1982; Hu and Sonnerup, 2002). Regarding the expansion speed, in an analysis of 37 ICMEs with clearly marked boundaries, Owens *et al.* (2005) find the following empirical relation between the rate at which the ICME radius is increasing (V_{EXP}) and the speed of the leading edge of the ICME (V_{LE}):

$$V_{\mathrm{EXP}}[\mathrm{km/s}] = 0.266\,V_{\mathrm{LE}}[\mathrm{km/s}] - 70.61 \tag{2}$$

For example, if $V_{\mathrm{LE}} = 500$ km/s, $V_{\mathrm{EXP}} = 62$ km/s, which means that at 1 AU the radial thickness of the ICME is growing at the rate of 124 km/s.

The next discriminator in the list is the cross-sectional shape of an ICME at 1 AU. The cross section of a CME as seen in a coronagraph near the Sun is roughly circular; thus, a zero-order expectation is that an ICME at 1 AU might be roughly circular, too. But the forces that act on an ICME in the direction of its motion are different than those acting perpendicular to its motion, so it is useful to consider an elliptical cross section as a first-order departure from circularity. Indirect methods suggest that the ratio of the major to minor axes of the cross section of an ICME at 1 AU might typically be less than 2 (based on a novel fitting procedure using the Grad-Shafranov equation, Hu and Sonnerup, 2002), whereas other analyses find a typical value closer to 4 [based on fitting multispacecraft observations (Mulligan and Russell, 2001) and on the ratio of the shock standoff distance to the ICME radial thickness (Russell and Mulligan, 2002)]. The ratio of major to minor ICME axes enters importantly in an analytical model in determining the values of the magnetic field strength and mass density within an ICME at 1 AU. Observationally, based on an average over 19 ICMEs, these numbers are $\sim$13 nT for field strength and $\sim$11 protons/cm^3 for number density (Lepping *et al.*, 2003), which completes the survey of relevant observations.

3.1.3. *An Analytical Model*

To repeat the main point, our goal is to give an equation of CME motion that captures the essential features of rapid acceleration from rest followed by slow deceleration, then to use it to show how different choices among its terms affect a CME's motion. The paradigm to follow for this Sun-to-Earth analytic approach is the treatments of van Tend and Kuperus (1978), van Ballegooijen and Martens (1989), Forbes and Isenberg (1991), and Chen (1996, 1997), which established the basic idea that a coronal magnetic flux rope anchored in the solar photosphere and in force-balance equilibrium can be destabilized by adding sufficient magnetic flux circulating around the central axis of the flux rope. Once destabilized, the flux tube expands in cross section and moves away from the Sun. The models mentioned above are more comprehensive than is needed here, since we are not concerned with the approach to destabilization (only what happens afterwards), and consequently we gain considerable simplicity by letting the flux tube encircle the Sun as a torus instead of anchoring of it in the photosphere. The approach is similar to those of Anzer (1978) and Kumar and Rust (1996). Under excess internal magnetic pressure the flux tube expands, and the force of expansion is balanced against the inertial reaction of the medium into which it is expanding. Under excess ambient pressure (particle plus magnetic) pushing up on its lower surface over that pushing down on its upper surface, the flux tube accelerates away from the Sun against the force of gravity and aerodynamic drag. This bottom-to-top ambient pressure excess minus the force of gravity can be thought of as a generalized buoyancy in the sense that it includes the magnetic pressure besides the usual hydrostatic pressure of the atmosphere. Thus, in words, the equations that describe the expansion and

propagation of the flux tube are

Expansion :

$$\text{(Ambient Mass Density)} \times \text{(Rate of Expansion)}^2 = \text{Pressure Inside} - \text{Pressure Outside} \tag{3}$$

Acceleration :

$$\begin{aligned}\text{(Mass of CME} + \text{Virtual Mass)} \times \text{Acceleration} &= \text{Force of Gravity} \\ &+ \text{Outside Magnetic \& Particle Pressure on Lower Surface Area} \\ &- \text{Same on Upper Surface Area} - \text{Drag Term}\end{aligned} \tag{4}$$

The two equations are coupled since the "Pressure Outside" term in the first equation changes as the flux tube moves through the ambient medium as governed by the second equation, and the bottom-to-top pressure differences that propel the CME in the second equation are determined by the expansion of the flux tube as governed by the first equation. "Virtual Mass" is a concept from hydrodynamics that allows one to express, by an appropriate increase in the mass of the body, the force needed to move the ambient medium out of the way as the body accelerates. For a cylindrical body, such as our ICME torus approximates, the virtual mass is the volume of the cylinder times the mass density of the ambient medium (*e.g.*, Le Méhauté, 1976, p. 177).

Although the physics behind the coupled expansion and propagation equations is simple, replacing the word terms with mathematical terms entails choices among various options in formulation. Most of these choices are fairly pedestrian, but the drag term and the ratio of major-to-minor axes of the ICME cross-section merit description.

3.1.4. *The Drag Term*

As mentioned in Section 3.1.2, Reiner *et al.* (2003) found that radio observations of the propagation of fast CMEs away from the Sun are inconsistent with drag terms that cause deceleration to decrease with distance from the Sun. The pertinent distinction is between a velocity-versus-distance profile that is concave downward (the Reiner *et al.* template) and one that is concave upward (after the peak in velocity near the Sun). Reiner *et al.* then point out that the standard form of the drag term gives profiles that are incorrectly concave upwards, which leads to the important conclusion that the standard form of the drag term evidently does not apply to CME propagation. The standard drag term has the form $C_D A \rho \, |V_{\rm CME} - V_{\rm SW}| \, (V_{\rm CME} - V_{\rm SW})$, where C_D is the drag coefficient (typically around unity), A is the cross-sectional area of the body, and $V_{\rm CME} - V_{\rm SW}$ is the relative velocity between the body and the medium though which it moves, in this case the CME moving through the solar wind. Vršnak and Gopalswamy (2002) show that the disagreement just mentioned between the Gopalswamy *et al.*/Reiner *et al.* templates and the standard drag term occurs also if the drag term is linear in the velocity difference instead of

quadratic. In either case, the primary reason that velocity-versus-distance profiles are concave upward after the velocity peak is that near the Sun the density, ρ, is large and the velocity difference, $V_{\mathrm{CME}} - V_{\mathrm{SW}}$, is also large, whereas these terms are small far from the Sun. That is, drag is strong near the Sun and weak farther out. The problem might go away, therefore, if for some reason the drag coefficient, C_D, should be compensatingly small near the Sun. Cargill *et al.* (1996) suggested a reason: C_D might be small near the Sun because the magnetic pressure greatly exceeds plasma pressure in this region. The idea is that a body moving fast through an ordinary fluid experiences drag as a result of the flow separating from the flanks of the body, leaving a low-pressure wake behind and so, consequently, a strong braking, fore-to-aft pressure difference. This is the situation to which the standard form of the drag term applies. By contrast when a strong magnetic field drapes fore-to-aft over the body as it moves, the field could force the plasma to flow all the way around the body without separating from it, thus leaving no low-pressure wake, which translates into a small drag coefficient.

Figure 6 illustrates the difference in velocity-versus-distance profiles that the two assumptions about C_D (variable or fixed) give. The three thin and (more or less) straight lines slanting downward to the right show examples of the Gopalswamy *et al.* template. They were obtained from equation (1) with initial velocities at 15 R_s of 500, 1000, and 1500 km/s. The thick lines show realizations of the word equation (3) in which initial parameters were chosen to give a peak speed near 1000 km/s. (For a discussion of a specification of initial CME and ambient coronal and solar wind conditions, see Chen (1996, 1997)). For the fixed C_D case (dashed line) the drag coefficient was held fixed at unity; for the variable C_D case (solid line) it was set equal to $\tanh \beta$, where β is the ratio of plasma pressure to magnetic pressure in

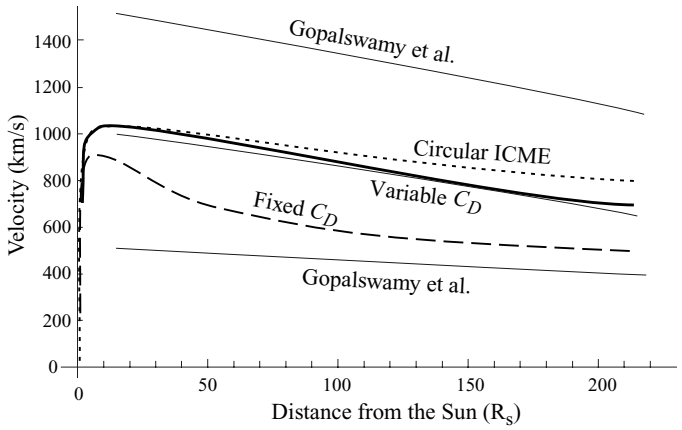

Figure 6. Velocity-versus-distance profiles showing three examples of the Gopalswamy *et al.* template from Equation (1) and three realizations of Equation (3) which differ from one another as labeled.

the ambient solar wind. $\tanh\beta$ is small near the Sun where the magnetic pressure greatly exceeds the plasma pressure, and it approaches unity away from the Sun, where the two pressures are comparable. (Other particulars of the realization of (3) that produced the curves in Figure 6 are given below.) The result demonstrates that the Cargill *et al.* suggestion of a small drag coefficient near the Sun indeed eliminates the concave upward shape of the curve seen in the fixed C_D case. Moreover, the variable C_D case follows the Gopalswamy *et al.* template (almost hidden by the thick line) reasonably well.

3.1.5. *Ratio of Major-to-Minor Axes and Other Values at 1 AU*

In Figure 6 the dotted line labeled "Circular ICME" illustrates by comparison with the "Variable C_D" curve two choices between the ratio of major to minor axes of the ICME cross section. It shows the case of no distortion of the initial circular cross section as the ICME moves outward; that is, the axis ratio is set to unity, although the radius increases according to Equation (3). The "Variable C_D" curve shows the case in which the axis in the direction of motion is determined by Equation (3) but the axis perpendicular to the direction of motion expands kinematically so that the angle subtended remains constant (Riley and Crooker, 2004). The result is a flattened, "pancake" shape, with the perpendicular axis 2.5 times longer than the axis in the direction of motion. Since the "Variable C_D" curve fits the Gopalswamy *et al*. template better than the "Circular ICME" curve, the comparison favors a ratio that is significantly bigger than unity. But it must be said that this result is not definitive since the "Circular ICME" case can be made to fit the Gopalswamy *et al.* template by doubling the drag term ($2\tanh\beta$); but then one needs an explanation for a larger-than-expected drag far from the Sun. Further support for a significantly-bigger-than-unity ratio of axes comes from comparing the mass density at 1 AU computed for the "Variable C_D" case ($17\,\mathrm{cm}^{-3}$) against the average value $\sim 11\,\mathrm{cm}^{-3}$. This is based on an initial radius of $0.1\,R_s$ and density of $3.5\times10^8\ \mathrm{cm}^{-3}$. The value for the "Circular ICME" case is $43\ \mathrm{cm}^{-3}$, which is too large. But this discrimination against a circular cross section is also somewhat soft because it could be changed by choosing a different initial density. Based on an initial magnetic field strength of 5 G, the computed value at 1 AU for both circular and elliptical cross section cases is 12 nT, which is essentially the same as the observed average value. The computed ICME speed at 1 AU is 677 km/s, and the computed expansion speed is 63 km/s, which is somewhat less than the 108 km/s value that the Owens *et al.* formula gives for a leading edge velocity of 677 km/s. Nonetheless, the computed front-to-back dimension of the ICME at 1 AU in the direction of motion is 0.25 AU, which compares favorably with observed typical values between 0.2 and 0.25 AU.

3.1.6. *Acceleration and Virtual Mass*

Recall that observed accelerations of CMEs in the inner corona vary from a few $\mathrm{m/s}^2$ up to $\sim$1000 $\mathrm{m/s}^2$. Figure 7 shows the computed acceleration in the inner corona using the same realizations of Equation (3) that generated the curves in Figure 6.

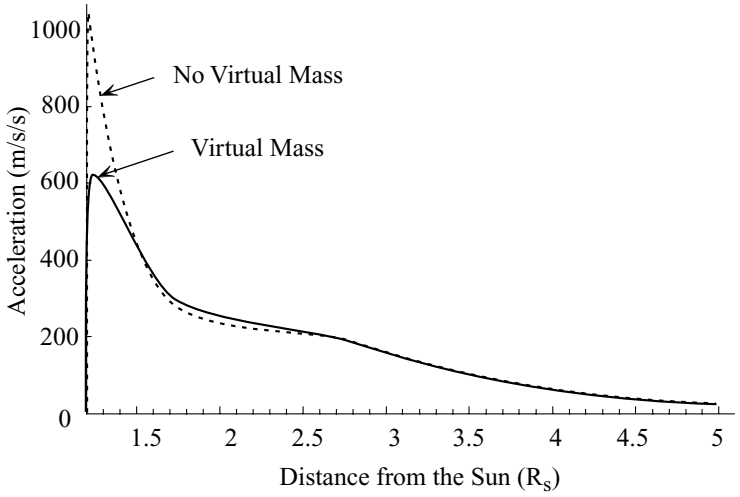

Figure 7. Computed accelerations in the inner corona for the cases of virtual mass and no virtual mass using the equations that generated the "Variable C_D" curve in Figure 6.

The figure illustrates that the simple generalized-buoyancy-versus-gravity-and-drag model that Equation (3) expresses can produce accelerations in the observed range. It also shows that adding virtual mass to the acceleration equation brings the peak acceleration into the observed range, but that after the initial peak, virtual mass has little effect on acceleration. This is because beyond about 1.5 R_s, ambient density, which makes up virtual mass, is relatively small. The initial peak in acceleration is perhaps non-physical since it results from an imposed pressure imbalance between the CME and the ambient medium. Thus, the value of about 200 m/s^2 that persists after the peak is the more appropriate value to use, and it happens to be the observed typical value. Figure 7 also demonstrates that generalized buoyancy is a strong force.

3.1.7. *Comparison with MHD Simulation*

Figure 8a shows a comparison between velocity-versus-distance profiles (out to 50 R_s) obtained from an MHD simulation of a CME (Riley *et al.*, 2003) and an analytic computation based on Equation (3) with initial parameters chosen to match the simulation. The two curves have the same general shapes. Differences in the ambient solar wind speeds cause the MHD simulation velocity to continue to rise at 50 R_s, whereas the analytical velocity remains flat. More importantly the maximum acceleration in the simulation ($\approx$32 m/s^2) is less than that in the analytical case ($\approx$200 m/s^2). Despite these differences, the comparison indicates that the same basic transport physics (expansion, generalized buoyancy, gravity, and variable drag) might operate in both cases.

Figure 8b shows that the MHD simulation generates an ICME cross section at 1 AU that is about twice as flat as that used in the analytical case. The central dimple

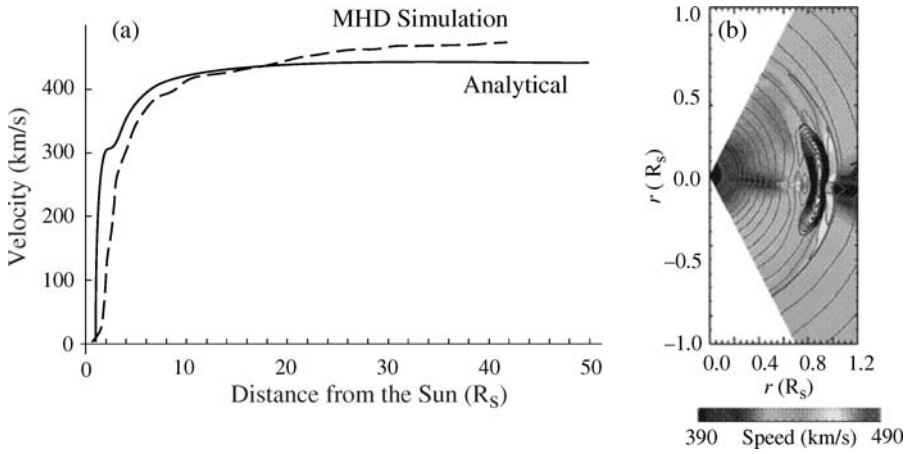

Figure 8. A comparison between analytical results and an MHD simulation of a CME. Panel (a) is the velocity-versus-distance, and panel (b) is the ICME shape at 1 AU.

in the ICME shape results from a higher equatorial density in the ambient solar wind, which might also account for its smaller equatorial thickness (∼0.14 AU) compared to the analytical case (0.24 AU).

3.1.8. *Conclusions*

The transport properties of fast, impulsive CMEs can be understood (as modeled analytically) by expansion under magnetic over-pressure leading to expulsion under generalized buoyancy, which can be much stronger than gravity. Drag appears to be weak near the Sun (possibly because of magnetic suppression of a low-pressure wake) but more-or-less normal farther out. Comparison between analytical results and an MHD simulation shows qualitative agreement on essential points.

3.2. Numerical MHD Modeling and Propagation

Because of their large-scale nature (Hundhausen, 1999), CMEs are amenable to treatment using MHD theory. Numerical models have been developed that are able to deduce their global features (see, *e.g.*, Detman *et al.*, 1991; Gosling *et al.*, 1998; Manchester *et al.*, 2004; Odstrcil and Pizzo, 1999a,b,c; Riley *et al.*, 1997; Vandas *et al.*, 1995, 1996; Wu *et al.*, 1995, 1997, 1999). One of these models (Cargill *et al.*, 1996, 2000) exploits the fact that an interplanetary CME can often be regarded, from a dynamic point of view, as being detached from its anchorage back at the Sun. Thus, as in the analytical model in Section 3.1, many aspects of CMEs can be modeled using an azimuthally-symmetric configuration corresponding to a toroidal magnetic flux rope with its axis of rotation running through the poles of the Sun.

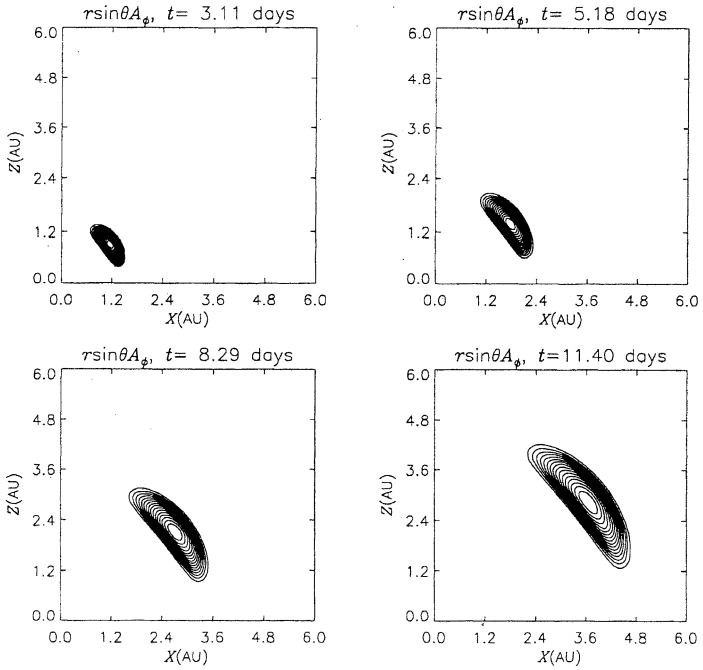

Figure 9. The magnetic field lines of the flux rope projected in the $r - \theta$ plane at four times during its progress from the Sun to 5 AU.

Here, we use the algorithms of Zalesak (1979) and DeVore (1991) to solve the MHD equations to an accuracy of fourth order in space and second order in time. The divergence of the magnetic field is kept at zero by using the vector potential to prescribe the magnetic field. The model is designed to investigate the evolution of magnetic flux ropes as they interact with the surrounding environment. Figure 9 shows the projection of the magnetic field lines of the flux rope in such a simulation. Contour lines of the vector potential are projected onto the x-z plane with x the in-ecliptic coordinate and z the coordinate in the direction of the rotational axis of the Sun. The flux rope has an internal overpressure initially, and as it propagates outwards, it loses its initial circular shape and becomes shell-like with a much larger extent in the meridional than in the radial direction. This is due to the smaller pressure gradient in the meridional direction.

Figure 10 shows the simulated plasma properties of the outward moving magnetic flux rope in a radial cut. The meridional component of the magnetic field B_θ shows a sine-like signal, whereas the azimuthal component of the magnetic field B_ϕ has a bell-like shape (with a molded hat). The latter corresponds to the winding of spiral field lines around the axis of the rope in the ϕ direction, where the height of a single winding increases when the spiral is closer to the axis. The radial velocity in the third panel also shows a sine-like signal, which corresponds to a

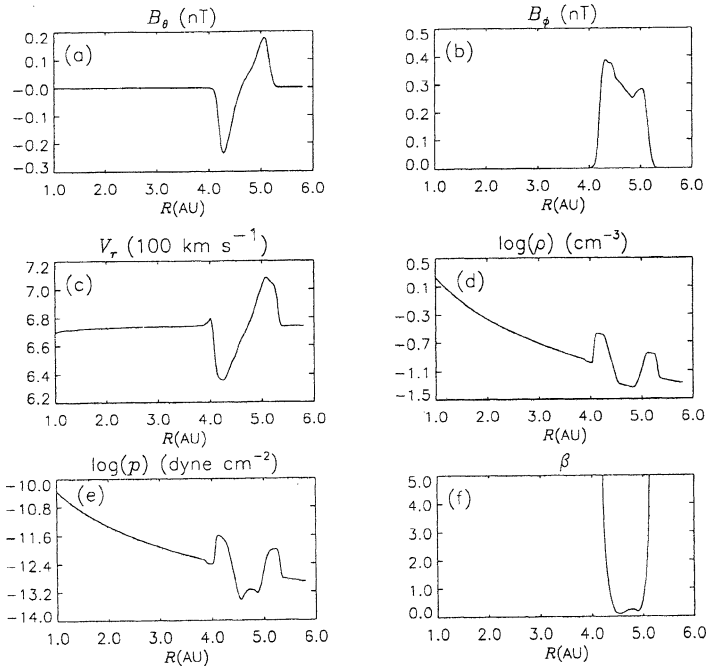

Figure 10. B_θ, B_ϕ, the radial velocity, plasma density and pressure, and plasma β at 11.4 days. Only the outer 200 cells of the simulation are shown.

forward and a reverse shock pair. In the fourth panel we see a density-signal with two bumps at the shocks. The density between those bumps is lower than the density outside the bumps, which is due to the overexpansion. The pressure-signal in the fifth panel shows a similar shape. Finally, the sixth panel shows the plasma β. The region within the CME is a region with low β, and so it is dominated by magnetic forces.

The interaction of CMEs can be studied with MHD simulations. During the active part of the solar cycle there are, on average, about four CMEs per day, so interactions between CMEs may be relatively common. A well-observed example of an interaction of this type occurred on January 10, 2000. Between 16:30 and 19:30 UT, the Radio and Plasma Wave Experiment (WAVES) on the Wind spacecraft (Bougeret *et al.*, 1995) detected an extremely narrow-band radio type II burst, which was flanked by intense radio type III bursts. That event was associated with a slow, dense CME being rammed from behind by a faster, less-dense CME, as observed by LASCO (Brueckner *et al.*, 1995) on SOHO (Gopalswamy *et al.*, 2001, 2002; see also Figure 16 in Forsyth *et al.* (2006), this volume). Since the radio signal outbursts are due to energetic electrons which may originate at shocks, it is useful to study the evolution and structure of the shocks that might form during the collision of the two CMEs. Figure 11 (Schmidt and Cargill, 2004) shows results for a

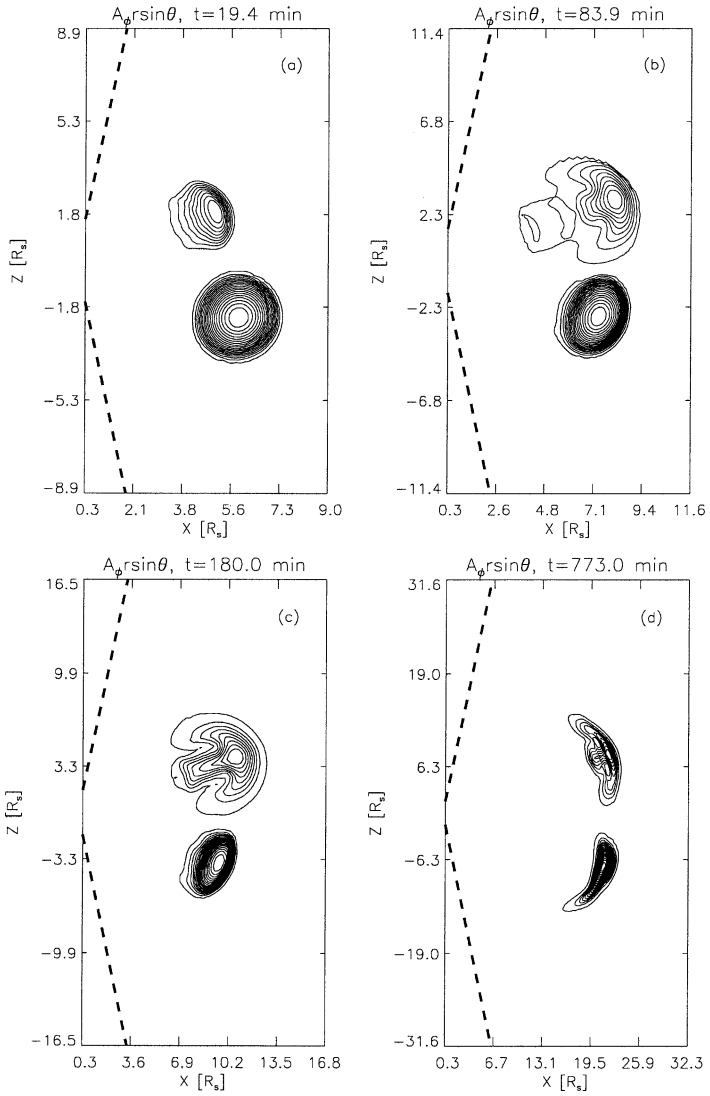

Figure 11. Contour plots of the vector potential at four times during the evolution of two colliding CMEs whose meridional angle is separated by 40° and that interact with each other by shock interaction (Adapted from Schmidt and Cargill, 2004).

simulation of the January 10, 2000 event. The simulation box, indicated by the thick dashed lines, comprises the field of view of the C2 and C3 coronagraphs, and the geometrical dimensions and velocities of the CMEs are taken from the coronagraph observations. After the fast, less-dense (upper) CME overtakes the slow, dense (lower) CME, the lower CME is deflected into the Southern hemisphere by its interaction with the forward shock in front of the fast CME. This shock impacts the

slow CME, causing it to flatten at its northern edge. The shock penetrates into the denser material of the slow CME, steepening significantly because of the reduced Alfvén speed there. We find that the steep shock that is generated within the slow CME is quite persistent. It could possibly serve as a site for the diffusive acceleration of particles if there is an adequate seed population of particles nearby. Additional examples of CME interactions that can be studied with MHD simulations can be found in Section 4 of Forsyth *et al.* (2006), this volume. These are reconnection with the ambient field and distortion caused by propagation into solar wind regions with different speeds.

4. Flux Rope Modeling and Fitting

C. CID, P. RILEY

On average, about one third of ICMEs identified in the solar wind contain a rotation in the magnetic field vector (Gosling, 1990). They are commonly called magnetic clouds (MCs, for more on clouds, see Wimmer-Schweingruber *et al.*, 2006, this volume). Their features in the solar wind, strong magnetic field, large rotation of the field vector and a low proton temperature indicate that they have a very well-defined magnetic field topology.

Richardson and Cane (2004) have found that the fraction of ICMEs that are also magnetic clouds varies during the course of the solar cycle from 15% at solar maximum to as much as 100% at solar minimum. Why only some ICMEs contain – or can be identified as – magnetic clouds remains unknown. Perhaps it is an observational selection effect: Whether one observes the necessary signatures to classify the event as a magnetic cloud may depend sensitively on the trajectory of the spacecraft through the structure. On the other hand, it may represent an evolutionary phenomena: simpler magnetic clouds interacting with one another may produce more complex ICMEs that do not retain the classic field rotations and enhancements and/or temperature depressions. Finally, it may suggest distinct birth mechanisms: non-cloud ICMEs are produced by one process, while clouds are produced by another. Numerical simulations currently favor the "selection effect" interpretation (Riley *et al.*, 2003). Whatever the relationship between ICMEs and magnetic clouds turns out to be, clouds are simpler to describe, parameterize, and model. As such, it makes sense to focus our efforts on understanding them first.

Several theoretical models have been proposed for the topology of magnetic clouds, but the procedure to check theoretical predictions from these models with experimental data is complicated. Although magnetic clouds are three-dimensional objects, the magnetic field vector cannot be measured at any desired point inside this structure. Experimental data are limited to a line tracing the trajectory of a spacecraft through the cloud as it travels away from the Sun. In this scenario,

the models have to take into account not only the magnetic field topology but also the position inside the magnetic cloud where those experimental data were obtained.

4.1. Approaches to the Problem

Magnetic field configurations for clouds were first proposed in the early 1980s. Burlaga *et al.* (1981) and Klein and Burlaga (1982) considered the possibility of magnetic field lines as a family of circles centered about the axis of the magnetic cloud. Suess (1988) proposed other pinch configurations, but all of them were incompatible with observations.

Goldstein (1983) considered magnetic clouds as force-free configurations, that is, the electric current is parallel to the magnetic field. Then, for static conditions the equation $\nabla \times \mathbf{B} = \alpha(r)\mathbf{B}$ is obtained. Several solutions to this equation were proposed. Burlaga (1988) considered $\alpha(r) = 1$, obtaining the cylindrically symmetric solution proposed by Lundquist (1950). With this solution, magnetic clouds are described as magnetic flux ropes, that is, cylindrical configurations with a two-component magnetic field, one along the axis of symmetry and another in the azimuthal direction. Lepping *et al.* (1990) fitted several examples of magnetic clouds. The procedure starts with a minimum variance analysis, which provides a starting value for the orientation of the axis. Then normalized magnetic field components are fitted with six free parameters related to size, boundaries, latitude and longitude of the axis, and the impact parameter (minimum distance between the spacecraft and the cloud's axis). Finally, the magnetic field strength is fitted, involving one more free-parameter, the magnetic field strength at the axis.

Experimental data show that the maximum of the magnetic field profile is often displaced towards the leading edge of the cloud. However, for the models described above, this maximum is located at the closest distance to the axis, that is, in the middle of the magnetic cloud time interval. More recently, other configurations have been proposed, such as spheromak solutions of the force-free equation (Ivanov and Kharshiladze, 1985; Vandas *et al.*, 1991, 1992, 1993) or toroidal solutions (Ivanov *et al.*, 1989; Romashets and Ivanov, 1991). Moreover, the static assumption was removed, and the effects of expansion and interaction with the ambient plasma were included (Osherovich *et al.*, 1993; Farrugia, 1995; Marubashi, 1997).

Pressure gradients have been observed inside MCs, indicating that they are not force-free structures. To address this, non force-free methods have been introduced. Mulligan and Russell (2001) proposed a model using exponential distributions for magnetic field strengths that can create both cylindrically symmetric and non-symmetric magnetic topologies. Ten parameters are used to describe a cylindrically symmetric flux rope. Seven are related solely to the

magnetic field topology and the other three to the orientation of the symmetry axis and to the impact parameter. For the non-symmetric topologies, the number of free parameters was increased to eleven.

Another analytical approach to modeling non-force-free magnetic clouds is to assume a current density vector and then solve Maxwell's equations for the magnetic field vector. Hidalgo *et al.* (2000) considered a cylindrical geometry with the axial and poloidal components of the current density constant and a null radial component. An improved version of this model shows the first fitting of thermal pressure inside a MC (Cid *et al.*, 2002; Hidalgo *et al.*, 2002a). Having taken into account the interaction of the cloud with the ambient solar wind, Maxwell's equations are solved in elliptical coordinates (Hidalgo *et al.*, 2002b). Projections of magnetic field lines on a cross section perpendicular to the axis are then ellipses, centered on the cloud axis. The expansion of magnetic clouds has been included by Hidalgo *et al.*, (2003), involving nine free parameters, four of them related to the orientation of the cloud and the spacecraft path.

The procedure followed to fit experimental data to these cloud models is to calculate the minimum of the sum of the residuals between the data and the model: $\chi^2 = \sum(B^2_{x,\mathrm{exp}} - B^2_{x,\mathrm{th}} + B^2_{y,\mathrm{exp}} - B^2_{y,\mathrm{th}} + B^2_{z,\mathrm{exp}} - B^2_{z,\mathrm{th}})$ where $B_{i,\mathrm{exp}}$, $(i = x, y, z)$ are the Cartesian components of the magnetic field observations in the cloud interval and $B_{i,\mathrm{th}}$, $(i = x, y, z)$ are the components of the theoretical model rotated into the frame of the observations.

Magnetic cloud properties have also been determined using the Grad-Shafranov reconstruction technique (Hu and Sonnerup, 2001, 2002). This method assumes that the cloud is an asymmetric cylindrical structure in approximate magnetostatic equilibrium. The structure perpendicular to its axis can be recovered using the Grad-Shafranov equation. With this technique, the boundaries of the cloud need not first be identified in the data.

Within the constraints of the caveats noted above, flux rope fitting (FRF) techniques can be an invaluable tool for extracting information about the properties of magnetic clouds. However, it has proven difficult to assess their accuracy from single-spacecraft data. In contrast, large-scale MHD simulations of CME evolution can provide both a global view as well as a localized time series at specific points in space. Riley *et al.* (2004) applied 5 different fitting techniques to 2 hypothetical time series derived from MHD simulation results (Figure 12). Independent teams performed the analyses of the events in "blind tests," for which no information, other than the time series, was provided. From the results, they inferred the following: (1) Accuracy decreases markedly with increasingly glancing encounters; (2) Correct identification of the boundaries of the flux rope can be a significant limiter; and (3) Results from techniques that infer global morphology must be viewed with caution. In spite of these limitations, FRF techniques appear to be a useful tool for describing in-situ observations of flux rope CMEs.

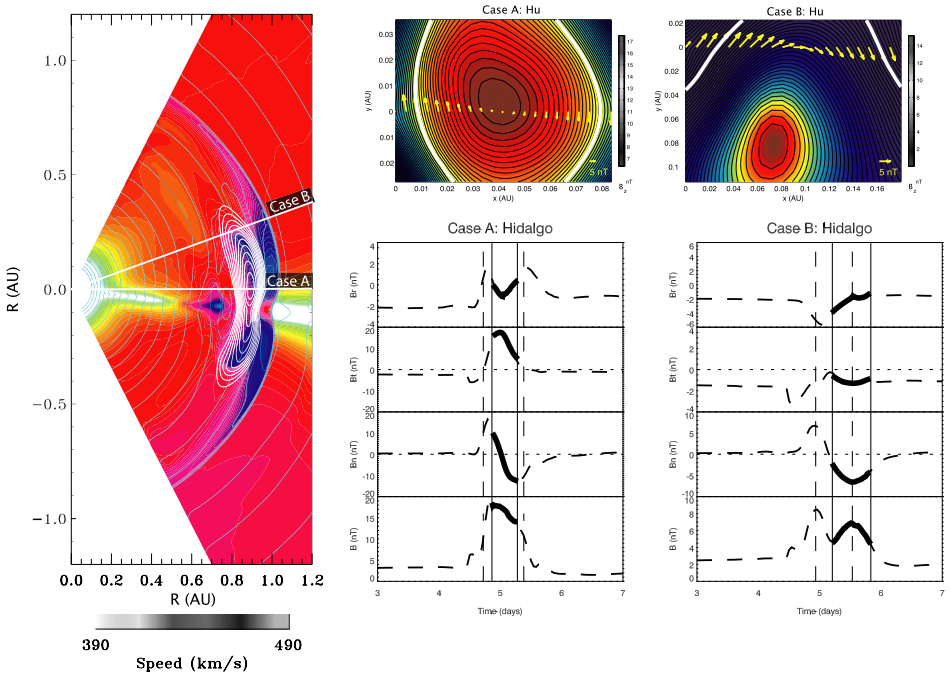

Figure 12. The left panel summarizes simulated arrival of flux rope CME to 1 AU. The two cases, labeled A and B were obtained by placing hypothetical spacecraft at these latitudes at a distance of 1 AU from the Sun. The fits obtained from the GSR technique are shown in the upper right and the fits obtained by the Current Density fitting technique of Hidalgo *et al.* are shown in the lower right.

4.2. Future Directions

A major unresolved issue with magnetic cloud models is that there is no independent way to assess the errors of the fit. One can and does, of course, compute deviations from the observed data with the derived profiles. In fact, minimizing this deviation defines the best fit to the data. But even a "reasonable" fit does not guarantee that the derived parameters and, moreover, the assumed field topology are "correct". The availability of data along at least two different lines inside the same magnetic cloud could help in this regard. At present, the models can reproduce the data measured at one spacecraft; however, the orientations inferred at other locations often do not appear to be consistent.

Using multipoint measurements of magnetic clouds requires extending the model to optimize magnetic cloud data from multiple spacecraft simultaneously. Noting that the theoretical models described above rely on a cylindrical approach, they could only be applied for observations for which the spacecraft are radially aligned. In this case, special care should be taken to obtain a global (non-local) magnetic field topology for the magnetic cloud.

Observations corresponding to the solar region associated with the CME should also be studied to verify the orientation of the magnetic cloud and the magnetic topology inferred from the model.

5. Shock Formation

G. MANN

5.1. OVERVIEW

Shock waves play an important role in the solar corona and interplanetary space, since they are able to accelerate particles (electrons, protons and heavy ions) up to high energies. Thus, shock waves accompanied by eruptive solar events are generally considered as one source of solar energetic particle events (SEP) (see Klecker *et al.*, 2006, this volume, and references therein). In the solar corona, shock waves can be produced either as blast waves due to the huge pressure pulse accompanying the flare and/or as piston driven shocks, *i.e.*, as a bow shock of a rising CME. It should be emphasized that a shock is a discontinuity well-defined in magnetohydrodynamics and, consequently, independent of the exciting agent. It represents a discontinuity with a transmitted mass flow, which is decelerated from a super-Alfvénic to a sub-Alfvénic speed. Thus, the shock is a dissipative structure, in which kinetic energy of a directed plasma flow is partly transferred to heating of the plasma. Since the necessary dissipation doesn't take place by means of particle collisions, these shocks are usually called collisionless shocks. The conservation laws lead to the well-known Rankine-Hugoniot relationships relating the quantities in the upstream region to those in the downstream region (Edmiston and Kennel, 1984). They result in an upper limit on the density and magnetic field jump across the shock, *i.e.*, $B_2/B_1 \leq N_2/N_1 \leq 4$, where B_2 and N_2 (B_1 and N_1) denote the magnitude of the magnetic field and the particle number density in the downstream (upstream) region.

5.2. SHOCK STRUCTURE

In-situ measurements by various spacecraft missions have revealed sub-structures of collisionless shocks in space plasmas. Generally, collisionless shocks can be divided into super- and sub-critical shocks as well as quasi-parallel and quasi-perpendicular shocks (see, *e.g.*, Kennel *et al.* (1985) and references therein). The critical fast Mach number M_f^* is defined by equating the normal component of the downstream flow velocity in the shock frame to the ordinary sound speed (Edmiston and Kennel, 1984). In contrast to sub-critical shocks ($M_f < M_f^*$; M_f, fast magnetosonic Mach number) resistivity in a super-critical shock ($M_f > M_f^*$) cannot provide all the dissipation necessary for a shock transition according to the Rankine-Hugoniot

relationships. M_f^* is strongly dependent on the upstream plasma β and the angle $\theta_{B,n}$. For low plasma β, as usually found under coronal circumstances, M_f^* varies between 1.5 and 2.7. Its maximum is 2.76 for $\theta_{B,n} = 90^\circ$ and vanishing plasma-β (Edmiston and Kennel, 1984). Thus, other processes like wave-particle interactions provide the dissipation required for fast magnetosonic, super-critical shock formation. This is the reason why such shocks are able to accelerate particles and are accompanied by large amplitude magnetic field fluctuations (Kennel *et al.*, 1985). If the angle $\theta_{B,n}$ between the upstream magnetic field and the shock normal is greater or smaller than 45°, the shock is called quasi-perpendicular or quasi-parallel, respectively. In the case of a quasi-perpendicular shock geometry, the shock transition has a typical scale length of a few ion inertial lengths, c/ω_{pi}, (corresponding to about 20 m in the corona at the altitude where the electron plasma frequency is 100 MHz and about 100 km in interplanetary space at 1 AU), where $\omega_{pi} = (4\pi e^2 N_p/m_p)^{1/2}$ is the proton plasma frequency, c is the speed of light, e is the elementary charge, N_p is the proton number density, and m_p is the proton mass. Immediately at the shock transition the magnetic field shows a so-called "overshoot," *i.e.*, the magnetic field is locally compressed to a maximum $B_{\max}$, which is higher than the downstream magnetic field B_2 ($< B_{\max}$) according to the Rankine-Hugoniot relationships. In the case of a quasi-parallel super-critical shock, its transition is extended up to a few hundreds of ion inertial lengths. It is accompanied by intermittent large-amplitude magnetic field fluctuations, the so-called SLAMS (Schwartz *et al.*, 1992; Mann *et al.*, 1994), in which the super-Alfvénic flow is partially decelerated.

5.3. Conditions Leading to Shock Formation

Generally, shocks are formed anytime a compressive wave is generated, since the nonlinear dynamics associated with the Reynolds stresses in the equation of motion cause such a wave to steepen with time. However, dissipation may damp the wave before a shock can form, so physically significant shocks tend to occur in regions where the velocity of the exciting agent exceeds the local fast magnetosonic speed v_f, which is related to the Alfvén speed v_A and sound speed c_s by $v_A \leq v_f \leq (v_A^2 + c_s^2)^{1/2}$. Consequently, the spatial behaviour of the Alfvén speed in the solar corona and interplanetary space is of interest, in order to evaluate where shock formation can take place. The origin of shock waves and their propagation through the corona and interplanetary space have been investigated by several authors (Gopalswamy *et al.*, 1997, 2000; Aurass *et al.*, 1998; Klassen *et al.*, 1999; Klein *et al.*, 1999) by evaluating dynamic radio spectra of type II radio bursts as signatures of shocks, radioheliographic observations, and X-ray images.

The Alfvén speed is defined by

$$v_A = \frac{B}{\sqrt{4\pi \mu \mathrm{m}_p N}}$$

with the magnetic field B and the full particle number density N. The symbol μ denotes the mean molecular weight, which has a value of 0.6 in the corona (Priest 1982). The electron number density N_e is related to the full particle number density N by $N = 1.92N_e$. Since v_A depends on the magnetic field B and the full particle number density N, a model of the magnetic field and the density in the corona and interplanetary space is needed for studying the radial behaviour of the Alfvén speed.

In the solar corona shock waves are established near but out of active regions (Aurass *et al.*, 1998, Klassen *et al.*, 1999; Klein *et al.* 1999; Gopalswamy *et al.*, 2000). Therefore, a one-fold Newkirk (1961) model

$$N_e(R) = N_0\, 10^{4.32 R_S/R}$$

($N_0 = 4.2 \times 10^4$ cm^{-3}; R_S, radius of the Sun) is chosen as an appropriate density model, since Koutchmy (1994) showed by white-light scattering observations that a this model fits well the conditions above quiet equatorial regions. Note that it corresponds to a barometric height formula with a temperature of 1.4×10^6 K, which is a typical value in the solar corona outside active regions. It is well known that the Newkirk model is a hydrostatic model and does not take into account the solar wind. To do so, Mann *et al.* (1999a) constructed a heliospheric density model as a special solution of Parker's (1958) wind equation. This model agrees very well with the observations from the corona out to 5 AU (see also Leblanc *et al.* (1994). Thus, the Newkirk model and the Mann *et al.* model are used for regions $R \leq 1.8R_S$ and $R \geq 1.8R_S$, respectively, with continuity at $R = 1.8R_S$. The radial behaviour of such a density model is presented in Figure 13.

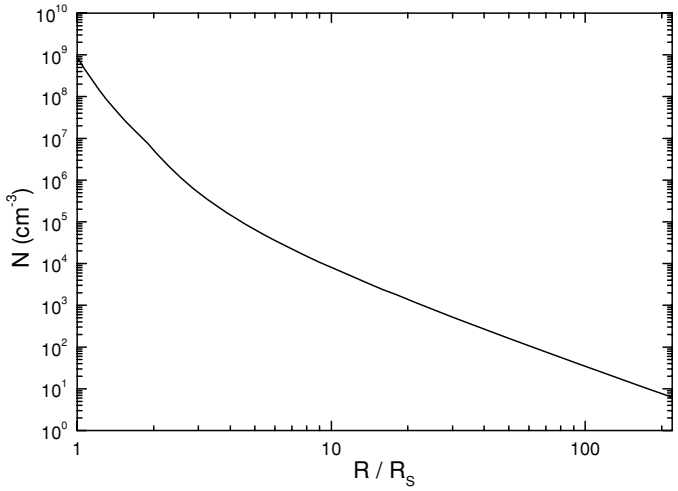

Figure 13. Radial behaviour of the electron number density according to the one-fold Newkirk (1961) model for the solar corona and the heliospheric density model by Mann *et al.* (1999a) for interplanetary space.

The model magnetic field **B** is composed of that of an active region $\mathbf{B}_{ar}$ and that of the quiet Sun $\mathbf{B}_{qS}$, *i.e.* $\mathbf{B} = \mathbf{B}_{ar} + \mathbf{B}_{qS}$. Here, an active region is modeled by a magnetic dipole with moment **M** and length λ. It is located at a depth $\lambda/2$ below the photosphere along the radial axis away from the center of the Sun. Then, the magnetic field of such a dipole is given by

$$\mathbf{B}_{ar} = \frac{3(\mathbf{M} \cdot \mathbf{r})\mathbf{r}}{r^5} - \frac{\mathbf{M}}{r^3} \tag{5}$$

where **r** denotes the distance from the center of the dipole. If B_0 is the magnitude of the magnetic field on the axis of the dipole, the magnetic moment is related to B_0 by $M = B_0\lambda^3/16$. Here, $B_0 = 0.8$ kG is taken as a typical value of the magnetic field in an active region (see Priest, 1982). The magnetic field of the quiet Sun is assumed to be radially directed so that its radial behaviour is given by

$$B_{qS} = B_S \left(\frac{R_S}{R}\right)^2 \tag{6}$$

This approach is appropriate outside the heliospheric current sheet (Banaszkiewicz *et al.*, 1998). The statistical analysis of coronal transient (or EIT) waves (Klassen *et al.*, 2000) provided a mean magnetic field of 2.2 G for the quiet Sun at the photosphere (Mann *et al.*, 1999b).

For this model of the Alfvén speed, the solar magnetic dipole defines a framework of cylindrical coordinates with an azimuthal symmetry, where the dipole is directed along the z-axis. The field magnitude, B, the full particle number density, N, and, subsequently, the Alfvén speed, v_A can be found at each point in the corona and interplanetary space. Figure 14 shows the radial behaviour of the Alfvén speed outward from the photosphere along a line inclined at 45° from the z-axis. The solid and dashed lines show cases in which the magnetic dipole is directed parallel (+ sign) and anti-parallel (− sign) with respect to that of the quiet Sun, respectively. For completeness, the dotted line represents the Alfvén speed due only to the quiet Sun field, *i.e.*, without any active region. Generally, a local maximum of the Alfvén speed of 740 km/s is found at 3.8 R_S. Furthermore, a local minimum of v_A is established in the middle of the corona. This minimum is strongly developed in the case of anti-parallel magnetic field orientation. A much more detailed discussion of this approach is given by Mann *et al.* (2003).

Of course, special values of the parameters (*e.g.*, B_0, B_S, and λ) have been used in this study. In reality they can change from case to case on the Sun. Nevertheless, the occurrence of a local minimum in the Alfvén speed near (but outside of) active regions in the middle of the corona and a local maximum of ≈800 km/s at distances 3–5R_S from the center of the Sun, *i.e.*, in the near-Sun interplanetary space, is the generally valid result of this study. This behaviour of the Alfvén speed has important consequences for the formation and development of shock waves in the corona and interplanetary space and their ability to accelerate particles. Inspecting the results by Edmiston and Kennel (1984), the first critical Mach number M_f^* is about 2 under

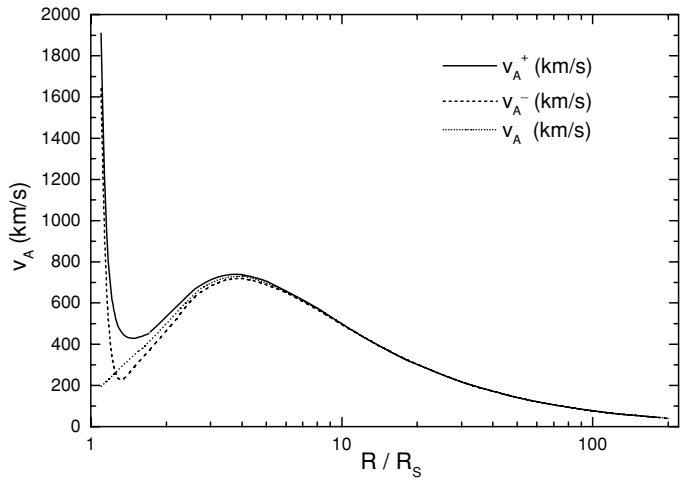

Figure 14. Alfvén speed along a straight line with $\delta = 45^\circ$ away from an active region as a function of the radial distance R. Further explanations are given in the text.

coronal circumstances. Thus, an agent exciting a super-critical, fast magnetosonic shock wave should have a velocity exceeding at least twice the Alfvén speed (see, also, Cairns *et al.* (2003)). Super-critical shocks are able to produce energetic particles, which are responsible for solar energetic particle events (Kahler, 1994; Reames *et al.*, 1996; Klein and Trottet, 2001; Vainio and Khan, 2004). Figure 14 implies that such shocks can be generated in the middle of the corona $\approx 1.2 - 2R_S$ and in interplanetary space beyond $\approx 8R_S$ (Gopalswamy *et al.*, 2001; Mann *et al.*, 2003).

6. Particle Acceleration and Transport

J. KÓTA, M. A. LEE, R. VAINIO

Particle acceleration is a fundamental feature of solar activity. It occurs at sites of magnetic reconnection in solar flares and at shocks driven by CMEs. These two sites appear to be responsible for the two classes of solar energetic particle (SEP) events observed in interplanetary space: impulsive and gradual events, respectively (see Mikić and Lee, 2006, this volume). Impulsive events have ion charge-state distributions characteristic of heated flare plasma. The particles in impulsive events are thought to be accelerated either by reconnection electric fields (Litvinenko, 1996), turbulence generated at the reconnection site (Emslie *et al.*, 2004), or at coronal shocks produced by reconnection jets or heating (Tsuneta and Naito, 1998). Impulsive events are not directly related to a CME and are not considered further in this section. However, CMEs are generally accompanied by flares arising from

changes in magnetic topology in the wake of the CME. Thus, gradual events which are observed on magnetic field lines favorably connected to the flare site may very well include a flare/impulsive component. The existence and/or importance of this component is currently controversial (Cane *et al.*, 2002, 2003; Tylka *et al.*, 2005).

6.1. Ion Shock Acceleration

A fast CMEs ($V_{\mathrm{CME}} \geq 10^3$ km/s) certainly drives a shock wave ahead of it. The strength of the shock may initially decrease but will increase beyond $\approx 4R_S$ as the Alfvén speed decreases, as described in Section 5.3 and Figure 14. This CME-driven shock is an ideal site for ion acceleration all the way to Earth orbit and beyond.

6.1.1. *Focused Transport Equation*

The focused transport equation, which is restricted to field-aligned transport of particles, is the starting point for most treatments of SEP transport and acceleration. The full version of the equation, appropriate to oblique or quasi-perpendicular shocks, may be written as (Skilling, 1971; Ruffolo, 1995; Isenberg, 1997; Kóta and Jokipii, 1997):

$$\begin{aligned}
&\frac{\partial f}{\partial t} + (V_i + w\,\mu b_i)\frac{\partial f}{\partial x_i} \\
&\quad + \left(\frac{1-\mu^2}{2}\right)\left[\frac{w}{L} - \frac{2}{w} b_i \frac{DV_i}{Dt} + \mu(\delta_{ij} - 3b_i b_j)\frac{\partial V_i}{\partial x_j}\right]\frac{\partial f}{\partial \mu} \\
&\quad + \left[-\frac{\mu b_i}{w}\frac{DV_i}{Dt} + \mu^2 b_i b_j \frac{\partial V_i}{\partial x_j} + \frac{1-\mu^2}{2}(\delta_{ij} - b_i b_j)\frac{\partial V_i}{\partial x_j}\right] p\frac{\partial f}{\partial p} \\
&= \frac{\partial}{\partial \mu}\left(\frac{D_\mu}{2}\frac{\partial f}{\partial \mu}\right) + q
\end{aligned} \tag{7}$$

where the particle speed, w, momentum, p, and the cosine of the pitch angle, μ are measured in the frame co-moving with the solar wind plasma at velocity, V_i. The symbol b_i represents the unit vector in the direction of the magnetic field, B_i, and L is the adiabatic focusing length ($1/L = b_i B^{-1} \partial B/\partial x_i$). The notation DV_i/Dt refers to the total derivative, *i.e.*, the acceleration of the fluid. For high particle speed ($w \gg V$), the DV_i/Dt terms can be neglected, and a relativistic correction appears for relativistic speed (Ruffolo, 1995).

This equation applies under broad conditions and remains valid for highly anisotropic pitch-angle distributions. Scattering may be either strong or weak, up to the scatter-free limit. The particle speed may be either higher or lower than the fluid speed. Terms of the order of $(V/w)^2$ can be neglected at high energies but may be of importance in the injection process. Particles in this description are assumed to remain tied to the field lines, reducing the spatial variation to one dimension,

so as to keep the computation at a tractable level. The drift motion of particles across the magnetic field is neglected, which should not be a severe omission if particle gradients across the field are small. The role of cross-field diffusion is still not fully understood and requires further theoretical efforts. Another, equivalent formulation of the same equation, written in conservation form, was considered by Ruffolo (1995).

A major difference from the spatial diffusion formulation of shock acceleration discussed in Section 6.1.2 below is that the acceleration rate depends on pitch-angle if the compression of the fluid is not isotropic. Particles moving along the field ($\mu \approx \pm 1$) sense compression parallel to the field, while particles moving at near 90° pitch angle ($\mu \approx 0$) sense compression perpendicular to the field. The compression rates in the two respective directions can be expressed in terms of the change in (n/B) and B, respectively (Kóta and Jokipii, 1997), and turn out to be different for parallel and perpendicular shocks. Here n is the plasma density. At a parallel shock, n (and hence n/B) changes, while B remains unchanged. A perpendicular shock, on the other hand, changes B but not (n/B).

The equation of focused transport has been solved by direct numerical methods but, also, may be solved by employing the Monte Carlo method (Kocharov *et al.*, 1998; Vainio *et al.*, 2000), where individual test particles are simulated under the guiding-center approximation in a given background field geometry. Particle scattering off turbulence and/or waves is simulated via a random generator by performing small-angle scatterings to the particle propagation direction in the frame co-moving with the scattering centers. This method is more time consuming than a finite difference scheme, but the advantage of the method is that it is flexible: once the scattering center velocities and background field geometries are specified, the method automatically yields the adiabatic and Fermi-mechanism particle energy changes. Thus, it has already been employed in studies of coronal (Vainio *et al.*, 2000) and interplanetary (Vainio, 1997) shock acceleration.

6.1.2. *Diffusive Shock Acceleration*

If scattering by turbulence is sufficiently strong to keep the particle distribution close to isotropic, the focused transport equation can be approximated by Parker's equation

$$\frac{\partial f_0}{\partial t} + V\frac{\partial f_0}{\partial s} - \frac{1}{A}\frac{\partial (AV)}{\partial s}\frac{p}{3}\frac{\partial f_0}{\partial p} = \frac{1}{A}\frac{\partial}{\partial s}\left(A\kappa_{\parallel}\frac{\partial f_0}{\partial s}\right) \tag{8}$$

where $f_0(s, p, t)$ is the isotropic part of the distribution function, s is the coordinate measured along the field lines, V is the speed of the scattering centers along the field lines, $A(s)$ is the flux-tube cross-sectional area, $\kappa_{\parallel} = \frac{1}{3}v\lambda_{\parallel}$ is the diffusion coefficient parallel to the field lines, and $\lambda_{\parallel}$ is the parallel scattering mean-free path. In this description, guiding-center drifts and perpendicular diffusion are also neglected. In a radial geometry, $s = r$ and $A = r^2$, and with a time-dependent radial solar wind speed, $V = V(r, t)$, this equation allows a simplified description of the

CME-driven shock as a propagating spherical discontinuity separating the ambient and the shocked plasma. With simplifying (and not very realistic) assumptions for κ_{rr} and V, it can be solved analytically (Lee and Ryan, 1986).

Let us consider a spherical shock wave propagating outwards from the Sun with a speed of V_s. If the mean free path is so short that the diffusion length, $\kappa_{\parallel}/V$, is shorter than the scale length of the system,

$$\kappa_{\parallel}/V \ll r, \tag{9}$$

the particle distribution around the shock position, $r = r_s(t)$, can be described in a one-dimensional geometry, *i.e.*,

$$\frac{\partial f}{\partial t} + u\frac{\partial f}{\partial x} - \frac{p}{3}\frac{\partial u}{\partial x}\frac{\partial f}{\partial p} = \frac{\partial}{\partial x}\left(\kappa_{xx}\frac{\partial f}{\partial x}\right), \tag{10}$$

where $\kappa_{xx} = \kappa_{\parallel}\cos^2\psi$ and $\psi = \sphericalangle(\mathbf{r}, \mathbf{B})$, $x = r_s - r$ is the local, co-moving coordinate along the shock normal pointing towards the shocked plasma, $u = \dot{r}_s - V$ and $\partial u/\partial x$ is negligible away from the shock. Thus, in a quasi-steady state, the distribution function can be obtained as a solution of a one-dimensional diffusion convection equation on both sides of the shock, and matching these solutions gives the canonical power-law spectrum of diffusive shock acceleration (see, *e.g.*, Vainio, 1999, for a review)

$$f(0, p) = \sigma\left[\frac{Q_0}{4\pi u_1 p_0^3} + \int_{p_0}^{p}\frac{dp'}{p'}\left(\frac{p'}{p_0}\right)^{\sigma} f_{-\infty}(p')\right]\left(\frac{p_0}{p}\right)^{\sigma}, \tag{11}$$

where u_1 is the upstream scattering-center speed along the shock normal, $\sigma = 3\rho/(\rho - 1)$ and ρ is the scattering-center compression ratio at the shock.[1] The first term describes particles injected into the acceleration process from low energies [from below the injection momentum p_0] at rate Q_0 [$\mathrm{cm}^{-2}\mathrm{s}^{-1}$], and the second term describes energetic particles of the ambient medium (distributed in momentum space as $f_{-\infty}(p)$) overtaken and re-accelerated by the shock.

The spectrum calculated at the shock holds in the downstream medium in the absence of adiabatic energy losses as well. In its derivation, however, one assumes that the system has an extent much larger than the diffusion length. This means that only a minor fraction of upstream ions may escape to the ambient medium. In the upstream region, the particle distribution decays exponentially with distance from the shock, *i.e.*,

$$f(x, p) = f(0, p)\exp\left(-\int_x^0 \frac{u_1\, dx}{\kappa_{xx}(x, p)}\right); \quad x < 0. \tag{12}$$

[1] Note that ρ does not necessarily equal the gas compression ratio of the shock. Vainio and Schlickeiser (1999) showed that for a low-Mach-number parallel shock, ρ can become very large if the downstream scattering centers are Alfvén waves transmitted from upstream.

If particles escape at some distance $L_1(p)$ ahead of the shock, *e.g.*, due to adiabatic focusing, and if the number of upstream diffusion lengths,

$$\eta(p) = \int_{-L_1(p)}^{0} \frac{u_1\, dx}{\kappa_{xx}(x,\, p)}, \tag{13}$$

is not large, the spectral form (for freshly injected ions) is (Vainio *et al.*, 2000)

$$f(0,\, p) = \frac{\sigma\, Q_0}{4\pi\, u_1\, p_0^3} \left(\frac{p_0}{p}\right)^{\sigma} \exp\left\{-\sigma \int_{p_0}^{p} \frac{dp'}{p'(e^{\eta(p')} - 1)}\right\}. \tag{14}$$

The rate of particle escape ahead of the shock into the flux tube is (Vainio *et al.*, 2000)

$$\frac{d^2 N_{\rm esc}}{dp\; dt} = \frac{u_1 A_s\, 4\pi p^2 f(0,\, p)}{e^{\eta(p)} - 1}, \tag{15}$$

where $A_s = A(r_s)$ is the flux-tube cross-sectional area at the shock. This spectral form is relevant to SEPs observed ahead of the CME-driven shock, if a quasi-stationary state in the vicinity of the shock can be assumed.

The steady-state spectrum holds up to a cut-off energy, E_c, determined by a balance between energy-losses and acceleration rate, by particle escape, or by the available acceleration time. The acceleration rate is determined by the rate of particle scattering near the shock, and the acceleration time scale at momentum p is

$$\tau(p) \equiv \frac{p}{\dot{p}} = \frac{\sigma}{u_1} \left(\frac{\kappa_{xx}(0-,\, p)}{u_1} + \frac{\kappa_{xx}(0+,\, p)}{u_2}\right). \tag{16}$$

In the downstream region, the turbulence is amplified from the upstream levels, and the mean free path is typically at least an order of magnitude shorter there than in the upstream region (Vainio and Schlickeiser, 1999). Thus, by neglecting the downstream contribution and equating the acceleration time scale with the dynamical time scale of the shock, $r_s/\dot{r}_s$, one gets an equation determining the cut-off momentum, p_c, as

$$\frac{\sigma \kappa_{xx}(0-,\, p_c)}{u_1^2} \approx \frac{r_s}{\dot{r}_s}. \tag{17}$$

The time scale for adiabatic deceleration is $\tau_{\rm ad} \sim (r/2V)$, producing a very similar cut-off momentum. Also particle escape by adiabatic focusing produces, apart from numerical constants, the same value for the cut-off momentum (Vainio *et al.*, 2000). Note, finally, that below the cut-off energy, the one-dimensional approximation is valid (*cf.*, Equattion (9)).

6.1.3. *Wave Excitation*

The SEP mean free path at 1 AU is observationally in the range 0.1–1 AU (Palmer, 1982; Dröge, 2000). If such values of $\lambda_\parallel$ were prevalent in the inner heliosphere and solar corona, as well, there would be no possibility for diffusive acceleration at

CME-driven shocks beyond 1-MeV energies. The accelerated particle distribution upstream of the shock front, however, is known to be unstable against generating hydromagnetic waves (Lee, 1983; Gordon *et al.*, 1999). The upstream particle scattering is, therefore, determined by the distribution of the particles themselves.

In steady state, the magnetic energy density of the unstable hydromagnetic waves is $W_B = \frac{1}{3} V_A \cos\psi (u_1 - V_A \cos\psi)^{-1} W_P$ (Gordon *et al.*, 1999), where V_A is the Alfvén speed and W_P is the energy density of the accelerated particles. By taking a sharpened resonance condition for the wave–particle interactions, *i.e.*, $k = m|\Omega_0|/p$, the wavenumber spectrum of the unstable waves is

$$\frac{k\, I(x,k)}{8\pi} \approx \frac{4\pi}{3} \frac{V_A \cos\psi}{u_1 - V_A \cos\psi} E\, p^3\, f(x,\, p), \tag{18}$$

where E is the particle energy. This gives an estimate for the mean free path of the energetic particles as

$$\lambda_\parallel(x,\, p) \approx \frac{v}{\Omega} \frac{2B^2}{\pi k I(k)} = \frac{v}{\Omega} \frac{2}{\pi} \left[\frac{u_1 - V_A \cos\psi}{V_A \cos\psi} \frac{B^2/8\pi}{(4\pi/3) E\, p^3\, f(x,\, p)} \right]. \tag{19}$$

where Ω is the ion gyro-frequency. To avoid non-linear wave amplitudes, the factor in brackets should be replaced by unity if its value gets smaller than this. For freshly injected particles ($f_{-\infty}(p) = 0$) with $p_0 = m u_1$ and $Q_0 = \varepsilon u_1 n_1$ (where ε is the fraction of the injected particles), we can use the spectrum at the shock, Equation (11), to estimate the upstream mean free path at the shock as

$$\lambda_\parallel(0-,\, p) \sim \frac{pc}{eB} \frac{2}{\pi} \left[\frac{3}{\sigma} \frac{M_A - \cos\psi}{\varepsilon M_A^2 \cos\psi} \frac{\frac{1}{2} m u_1^2}{E} \left(\frac{p}{m u_1} \right)^{\sigma - 3} \right], \tag{20}$$

and the bracketed quantity is seen to decrease with non-relativistic (relativistic) energy for shocks with $\sigma < 5$ (4), *i.e.*, $\rho > \frac{5}{2}$ (4). Particles accelerated by strong shocks are, thus, very efficient in generating upstream waves.

Using Equations (17) and (20) and $\frac{1}{2} v p = E$ gives the cut-off momentum of the shock accelerated particles as

$$\left(\frac{p_c}{m u_1} \right)^{\sigma - 3} \approx \frac{r_s}{\dot{r}_s} \frac{\pi e B_s}{2mc \cos\psi} \frac{\varepsilon M_A^2}{M_A - \cos\psi} = \frac{1.4 \times 10^7}{V_{s8} \cos\psi} \frac{\varepsilon M_A^2}{M_A - \cos\psi} \frac{r_\odot}{r_s}, \tag{21}$$

where V_{s8} is the shock speed in 1000 km s^{-1} = 10^8 cm s^{-1}. Thus, shocks in the outer solar corona with $V_{s8} \approx 1$, $u_1 \approx 1000$ km s^{-1}, $r_s \approx 5\ r_\odot$, $M_A \approx 2$, $\cos\psi \approx 1$, $\sigma \approx 5$, and $\varepsilon \approx 0.01$ can accelerate particles up to relativistic energies ($p_c \approx 1$ GeV/c).

Apart from some numerical factors, Equation (21) is the same as that used by Rice *et al.* (2003) in a study of CME shock acceleration. These authors performed MHD simulations of shock propagation through the inner heliosphere. They computed the energy spectrum at the shock by using an injection energy equal to 50% of the downstream thermal energy and the maximum momentum calculated from the dynamical time scale, similar to the above analysis. These spectra were then

allowed to convect to the downstream region by applying adiabatic deceleration, and to diffuse upstream of the shock front. These authors arbitrarily took $\eta(p) = 4$ at all momenta and, thus, calculated the flux of particles escaping to the ambient medium. In a parallel study, Li *et al.* (2003) used this particle injection for a focused transport simulation in a relatively undisturbed solar wind. These computations could qualitatively reproduce the essential features of CME-related SEP events.

The mean free path obtained above corresponds to the quasi-stationary state. Vainio (2003) studied the initial phase of wave generation ahead of the shock wave and showed that the escaping particle flux in case of a very strong moving source, like a strong CME-driven shock, would have a plateau-type power-law spectrum with a hard spectrum $dN_{\rm esc}/dp \propto p^{-1}$, indicating that $e^{\eta} - 1 \propto p^{3-\sigma}$, *cf.*, Equation (15). Without any free parameters, the particle escape model of Vainio (2003) could reproduce the SEP source profile deduced for the large 19 Oct 1989 SEP event at energies around 10 MeV. The model also predicted that wave generation in the solar corona during more typical small gradual events with 1-MeV-proton peak intensities below 10 $(\mathrm{cm}^2\ \mathrm{s\ sr\ MeV})^{-1}$, often associated with slower ($<$1000 km s^{-1}) CMEs, would be negligible. For such events, diffusive shock acceleration in the low corona ($r < 2\,r_{\odot}$) by refracting shock waves was studied by Vainio and Khan (2004). They showed that high-frequency Alfvén waves emitted from the solar surface and related to coronal ion-cyclotron heating would be able to provide enough scattering to accelerate protons up to tens of MeVs. The spectra of escaping particles would be consistent with those observed during typical small gradual events. Note that in the case of external upstream turbulence, η is usually a rapidly decreasing function of momentum, and the spectrum of the particles escaping to the upstream region is severely modulated (*cf.*, Equation (15)). Thus, in this case models connecting the observer to the downstream region are favored.

6.2. Ion Injection at Shocks

The distribution function described by Equation (11) depends on the injection rate Q_0, which cannot be determined from Equation (8), or even Equation (7). Equation (8) is restricted to energies much greater than u_1; Equation (7) presumes diffusive transport in μ which may not be valid for the scattering of particles with $v \approx u_1$ by the electromagnetic fluctuations at the shock front. Similarly the behavior of particles with $v \approx u_1$ in the advected distribution, $f_{-\infty}(p)$, is not well-described by Equation (11). The first-order Fermi mechanism may or may not operate for these low-energy particles, or it may operate for a small fraction of the advected particles. At the quasi-parallel Earth's bow shock or interplanetary traveling shocks, $\approx 10^{-2}$ of the incident solar wind ions are typically "injected" into the process of diffusive shock acceleration (Lee, 1982; Gordon *et al.*, 1999).

The behavior of the low-energy ions at a shock can best be revealed by numerical simulations (Scholer *et al.*, 2000), although injection is likely to be sensitive

to the assumed dimensionality of the simulation. Monte Carlo calculations using prescribed scattering mean free paths are conceptually instructive but are overly simplified (Ellison *et al.*, 1990). Malkov (1998) has presented an analytical theory of injection at a parallel shock based on a simplified version of Equation (7) with diffusive transport in μ.

A question of considerable importance is the energy threshold for diffusive shock acceleration as a function of ψ; that is, above what energy does first order Fermi acceleration occur as described by Equation (8)? At lower energies particle mobility normal to the shock is too small to allow particles to scatter back and forth across the shock, and they are swept downstream. A reasonable choice for the threshold speed is $u_1/\cos\psi$ in the upstream plasma frame. A particle with such a speed is kinematically able to escape the shock in the upstream direction by moving along the ambient field with $|\mu| = 1$. For quasi-perpendicular shocks, perpendicular diffusion can substantially reduce this threshold speed (Giacalone, 2005), but the actual reduced value is controversial. The threshold speed determines the mix of solar wind and ambient suprathermal/energetic particles accelerated at the shock, which in turn determines SEP composition (Tylka *et al.*, 2005). That the threshold energy increases markedly with ψ is shown by the decrease in ion intensity as ψ increases and the overall irregularity of ion intensity at quasi-perpendicular shocks (van Nes *et al.*, 1984).

6.3. Electron Shock Acceleration

In principle, electrons satisfy the same Equations (7) and (8) as do ions, and are subject to the process of diffusive shock acceleration. However, by virtue of their large speed and no established instability to enhance their pitch-angle scattering rate, $\kappa_\parallel$, is large, and the process is correspondingly slow. As a result, energetic electron enhancements at shocks are not large. An exception is at nearly perpendicular shocks where a single reflection of an electron, by mirroring in the region of increased magnetic field strength at the shock (the "shock drift" mechanism), can lead to substantial energy gain. Such electrons are observed at Earth's bow shock adjacent to the magnetic field line tangent to the shock surface (Wu, 1984). This mechanism is responsible for the unstable electron beams which excite type II radio bursts (see Pick *et al.*, 2006, this volume). The origin of the solar energetic electron beams in interplanetary space is controversial but it may be coronal shocks (Haggerty and Roelof, 2001; Ellison and Ramaty, 1985).

6.4. Temporal and Spatial Variations

An important aspect of CME-driven shock acceleration is the inherent temporal and spatial variation of the resulting SEP events. The driven shock first forms, then strengthens as the coronal Alfvén speed decreases, and finally weakens as the shock

expands into the heliosphere. The shock is also generally stronger near the nose and weaker on the flanks, which contributes to a dependence of particle intensity on magnetic field line geometry. As an observer's field line sweeps across the shock surface with increasing time, shock strength and ψ change. These variations were recognized by Cane *et al.* (1988) and invoked to argue for a shock origin of SEP events. In addition, ions escaping the shock upstream undergo a transition from scatter-dominated transport adjacent to the shock to nearly scatter-free transport further from the shock. This transition leads to a marked temporal variation in the ion intensity, energy spectrum and anisotropy as an event approaches the observer. In principle these variations provide information on shock geometry and ion transport. Current models attempt to include some of these features (Sokolov *et al.*, 2004).

6.5. CHALLENGES

The origin of SEPs at CME-driven shocks can account for most of the observed features of these events. Also the basic theoretical concepts are quite well understood. Nevertheless, there are several challenges to developing a complete theory:

(i) The intensity of upstream escaping ions and the high-energy cutoff are very sensitive to the form of the upstream excited wave spectrum. The wave spectrum needs to be calculated carefully with the correct resonance condition.
(ii) The transition from scatter-dominated ion transport adjacent to the shock to nearly scatter-free transport further away must be handled properly (Lee, 2005).
(iii) Ion injection from both the solar wind and the ambient suprathermal/energetic ion population must be included with appropriate thresholds and injection rates.
(iv) The role of perpendicular diffusion at quasi-perpendicular shocks needs to be assessed including possible instabilities and its influence on injection thresholds.
(v) The compression ratio, which plays a central role in the theory of diffusive shock acceleration, is the average-wave-frame compression ratio, which can be quite different from the plasma-frame compression ratio for these generally weak shocks. This issue must be addressed for oblique shocks including the determination of the downstream average-wave-frame.
(vi) The transport of SEPs downstream of the shock similarly transitions from scatter-dominated to nearly scatter-free as the turbulence decays, ions fill the inner heliosphere, and they cool adiabatically (Reames *et al.*, 1996; Lee, 2005). This transition needs to be included quantitatively with appropriate turbulence decay rates.

(vii) Several current models include time-dependence under an adiabatic approximation (Zank *et al.*, 2000; Lee, 2005), which is not valid at early times and high energies. The approximation needs to be relaxed.

7. Concluding Remarks

Future progress in understanding the origin and evolution of CMEs depends critically on obtaining new observations. More information is needed about the structure of the magnetic field in the corona before and after eruption. The magnetic field in the lower corona plays a fundamental role in the genesis of CMEs. Equally important are new observations of the magnetic field in the solar wind. Knowledge of how this field is distributed in space as a function of time would resolve several outstanding issues about CMEs and ICMES. Thus, ongoing efforts to improve vector magnetic field observations of the solar surface and to obtain multi-spacecraft observations of the interplanetary field need to be sustained. High resolution images of plasma structures in the corona and chromosphere also provide information about the coronal magnetic field because the low plasma β conditions there cause gradients in the plasma properties to be strongest in the direction perpendicular to the magnetic field. Virtually all of the evidence for the existence of neutral points and current sheets in the corona is based on such images.

More accurate observations are needed of the acceleration profile of CMEs and associated structures at altitudes below one solar radius where the strongest acceleration occurs. Because acceleration is proportional to the force acting on the plasma, such observations provide a strong constraint on theories of CME initiation. For example, initiation mechanisms based on ideal-MHD processes predict that the peak acceleration will occur at a time on the order of the Alfvén time scale of the erupting region, which is typically no more than a few minutes. Thus, models of this type may not be able to account for slowly accelerating CMEs which take several hours to reach their peak value (Zhang *et al.*, 2004). The various models also predict different reconnection signatures. While all the models, predict reconnection to occur after CME onset, some also require it before onset (*e.g.* Moore and Roumeliotis, 1992; Antiochos *et al.*, 1999).

Multi-spacecraft, in-situ observations of ICMEs are needed to resolve issues about the large scale structure of the magnetic field ejected during a CME. Such observations have already shown that the erupted field is in the form of a flux rope, but the distribution of the current density within the flux rope, and the overall structure along the axial field are not well known. Furthermore, the interaction of magnetic field of the ICME with the ambient field of the corona is not well understood. The long term fate of ICMEs in the outer heliosphere is also an unsolved question. Beyond about 10 AU, it is difficult to identify individual ICMEs, and it is thought that they merge together with CIRs to form GMIRs. Compositional

measurements with multiple spacecraft would also be a great help in sorting out the distinction between impulsive and gradual particle events.

Acknowledgments

This work was supported at the University of New Hampshire in part by grants ATM-0327512, ATM-0422764, and ATM-0518218 from the US National Science Foundation; NASA grants NNH05-AA131 and NNG05-GL40G, and the US Dept. of Defense MURI program on Space Weather. Work at SAIC was supported by the NASA LWS, SR&T, and SECTP programs, and by NSF through the SHINE program and the Center for Integrated Space Weather Modeling.

References

Aly, J. J.: 1984, *Astrophys. J.* **283**, 349–362.
Aly, J. J.: 1991, *Astrophys. J.* **375**, L61–L64.
Amari, T., Luciani, J. F., Mikić, Z., and Linker, J. A.: 2000, *Astrophys. J.* **529**, L49–L52.
Amari, T., Luciani, J. F., Aly, J. J., Mikić, Z., and Linker, J. A.: 2003, *Astrophys. J.* **585**, 1073–1086.
Amari, T., Luciani, J. F., Aly, J. J., Mikić, Z., and Linker, J. A.: 2003, *Astrophys. J.* **595**, 1231–1250.
Antiochos, S., DeVore, C., and Klimchuk, J.: 1999, *Astrophys. J.* **510**, 485–493.
Antiochos, S. K., and DeVore, C. R.: 1999, in: *Magnetic Helicity in Space and Laboratory Plasmas: Geophysical Monograph 111*, M. R., Brown, R. C., Canfield and A. A. Pevtsov (eds.), Amer. Geophys. Union, Washington, DC, p. 187.
Antiochos, S. K.: 1998, *Astrophys. J.* **502**, L181–L184.
Anzer, U.: 1978, *Solar Phys.* **57**, 111–118.
Aulanier, G., DeLuca, E. E., Antiochos, S. K., McMullan, R. A., and Golub, L.: 2000, *Astrophys. J.* **540**, 1126–1142.
Aurass, H., Hofmann, A., and Urbarz, H.-W.: 1998, *Astron. Astrophys.* **334**, 289–302.
Banaszkiewicz, M., Axford, W. I., and McKenzie, J. F.: 1998, *Astron. Astrophys.* **337**, 940–948.
Birn, J., Forbes, T. G., and Schindler, K.: 2003, *Astrophys. J.* **588**, 578–585.
Biskamp, D., and Welter, H.: 1989, *Solar Phys*. **120**, 49–77.
Bougeret, J.-L., Kaiser, M. L., Kellogg, P. J., Manning, R., Goetz, K., Monson, S. J., *et al.*: 1995, *Space Sci. Rev.* **71**, 231–263.
Brueckner, G. E., Howard, R. A., Koomen, M. J., Korendyke, C. M., Michels, D. J., Moses, J. D., *et al.*: 1995, *Solar Phys.* **162**, 357–402.
Burlaga, L.: 1981, *J. Geophys. Res.* **86**, 6673–6684.
Burlaga, L.: 1988, *J. Geophys. Res.* **93**, 7217–7224.
Cairns, I. H., Knock, S. A., Robinson, P. A., and Kuncic, Z.: 2003, *Space Sc. Rev.* **107**, 27–34.
Cane, H. V., Reames, D. V., and von Rosenvinge, T. T.: 1988, *J. Geophys. Res.* **93**, 9555–9567.
Cane, H. V., Erickson, W. C., and Prestage, N. P.: 2002, *J. Geophys. Res.* **107**, Issue A10 CiteID 1315 DOI 10.1029/2001JA000320.
Cane, H. V., von Rosenvinge, T. T., Cohen, C. M. S., and Mewaldt, R. A.: 2003, *Geophys. Res. Lett.* **30**, Issue A12 CiteID 8017, DOI 10.1029/2002GL016580.
Cargill, P. J., Chen, J., Spicer, D. S., and Zalesak, S. T.: 1996, *J. Geophys. Res.* **101**, 4855–4870.
Cargill, P. J., Schmidt, J. M., Spicer, D. S., and Zalesak, S. T.: 2000, *J. Geophys. Res.* **105**, 7509–7520.

Chen, J., Santoro, R. A., Krall, J., Howard, R. A., Duffin, R., Moses, J. D., *et al*.: 2000, *Astrophys. J.* **533**, 481–500.
Chen, P. F., Shibata, K., and Yokoyama, T.: 2001, *Earth, Planets and Space* **53**, 611–614.
Chen, J.: 1989, *Astrophys. J.* **338**, 453–470.
Chen, J.: 1996, *J. Geophys. Res.* **101**, 27499–27519.
Chen, J.: 1997, *Coronal Mass Ejections. Geophys. Monograph 99*, N., Crooker, J. A., Joselyn and J. Feynman (eds.), Amer. Geophys. Union, Washington, DC, pp. 65–81.
Chen, J., Howard, R. A., Brueckner, G. E., Santoro, R., Krall, J., Paswaters, S. E., St. Cyr, O. C., Schwenn, R., Lamy, P., and Simnett, G. M.: 1997, *Astrophys. J.* **490**, L191–L194.
Cheng, C. Z., Ren, Y., Choe, G. S., and Moon, Y.-J.: 2003, *Astrophys. J.* **596**, 1341–1346.
Cid, C., Hidalgo, M. A., Nieves-Chinchilla, T., Sequeiros, J., and Viñas, A. F.: 2003, *Solar Phys.* **207**, 187–198.
Detman, T. R., Dryer, M., Yeh, T., Hun, S. M., Wu, S. T., and McComas, D. J.: 1991, *J. Geophys. Res.* **96**, 9531–9540.
DeVore, C. R.: 1991, *J. Comput. Phys.* **92**, 142–160.
Dröge, W.: 2000, *Astrophys. J.* **537**, 1073–1079.
Dryer, M., Wu, S. T., Steinolfson, R. S., and Wilson, R. M.: 1979, *Astrophys. J.* **227**, 1059–1071.
Edmiston, J. P., and Kennel, C. F.: 1984, *J. Plasma Phys.* **32**, 429–443.
Ellison, D. C., Möbius, E., and Paschmann, G.: 1990, *Astrophys. J.* **352**, 376–394.
Ellison, D. C., and Ramaty, R.: 1985, *Astrophys. J.* **298**, 400–408.
Emslie, A. G., Miller, J. A., and Brown, J. C.: 2004, *Astrophys. J.* **602**, L69–L72.
Fan, Y.: 2005, *Astrophys. J.* **630**, 543–551.
Farrugia, C. J., Osherovich, V. A., and Burlaga, L. F.: 1995, *J. Geophys. Res.* **100**, 12293–12306.
Forbes, T. G.: 1990, *J. Geophys. Res.* **95**, 11919–11931.
Forbes, T. G., and Isenberg, P. A.: 1991, *Astrophys. J.* **373**, 294–307.
Forbes, T. G., Priest, E. R., and Isenberg, P. A.: 1994, *Solar Phys.* **150**, 245–266.
Forbes, T. G., and Priest, E. R.: 1995, *Astrophys. J.* **446**, 377–389.
Forbes, T. G.: 2000, *J. Geophys. Res.* **105**, 23153–23165.
Forsyth, R. J., Bothmer, V., *et al*.: 2006, *Space Sci. Revs.*, this volume.
Gary, G. A., and Moore, R. L.: 2004, *J. Geophys. Res.* **611**, 545–556.
Giacalone, J.: 2005, *Astrophys. J.* **628**, L37–L40.
Gibson, S. E., and Low, B. C.: 1998, *Astrophys. J.* **493**, 460–473.
Goldstein H.: 1983, M. Neugebauer (ed.), *Solar Wind Five*, *NASA Conf. Publ.* **CP-2280**, Washington, DC, pp. 731–733.
Gopalswamy, N., Lara, A., Lepping, R. P., Kaiser, M. L., Berdichevsky, D., and St. Cyr, O. C.: 2000, *Geophys. Res. Lett.* **27**, 145–148.
Gopalswamy, N., Yashiro, S., Kaiser, M. L., Howard, R. A., and Bougeret, J. L.: 2001, *Astrophys. J.* **548**, L91–L94.
Gopalswamy, N., Yashiro, S., Michalek, G., Kaiser, M. L., Howard, R. A., Reames, D. V., *et al.*: 2002, *Astrophys. J.* **572**, L103–L106.
Gopalswamy, N., Kundu, M. R., Manoharan, P. K., Rauolt, A., Nitta, A., and Zarka, P.: 1997, *Astrophys. J.* **486**, 1036–1048.
Gopalswamy, N., Kaiser, M. L., Sato, J., and Pick, M.: 2000, R., Ramaty and N.,, Mandzhavidze (eds.), *High Energy Physics: Anticipating HESSI*, *PASP Conf. Ser.* **206**, San Francisco, pp. 351–360.
Gopalswamy, N., Lara, A., Kaiser, M. L., and Bougeret, J.-L.: 2001, *J. Geophys. Res.* **106**, 25261–25273.
Gordon, B. E., Lee, M. A., Möbius, E., and Trattner, K. J.: 1999, *J. Geophys. Res.* **104**, 28263–28277.
Gosling, J. T.: 1990, in: C. T., Russell, E. R., Priest and L. C. Lee (eds.), *Physics of Magnetic Flux Ropes Geophys. Monograph 58*, Amer. Geophys. Union, Washington, DC, pp. 343–364.

Gosling, J. T., Riley, P., McComas, D. J., and Pizzo, V. J.: 1998, *J. Geophys. Res.* **103**, 1941–1941.
Haggerty, D. K., and Roelof, E. C.: 2001, *Proc. 27th Internat. Cosmic Ray Conf. (Hamburg)* **8**, 3238–3241.
Harrison, R.: 1986, *Astron. Astrophys.* **162**, 283–291.
Hidalgo, M. A.: 2003, *J. Geophys. Res.* **108**, Issue A8 CiteID 1320 DOI 10.1029/2002JA009818.
Hidalgo, M. A., Cid, C., Medina, J., and Viñas, A. F.: 2000, *Solar Phys.* **194**, 165–174. 10.1029/2001GL013875.
Hidalgo, M. A., Cid, C., Viñas, A. F., and Sequeiros, J.: 2002a, *J. Geophys. Res.* **107**, Issue A1 CiteID 1002 DOI 10.1029/2001JA900100.
Hidalgo, M. A., Nieves-Chinchilla, T., and Cid, C.: 2002b, *Geophys. Res. Lett.* **29**, Issue 13 CiteID 1637 DOI
Hu, Q., and Sonnerup, B. U. Ö.: 2001, *Geophys. Res. Lett.* **28**, 467–470.
Hu, Q., and Sonnerup, B. U. Ö.: 2002, *J. Geophys. Res.* **107**, Issue A7 CiteID 1142, DOI 10.1029/2001JA000293.
Hundhausen, A. J.: 1999, in:Strong, K. T., Saba, J. L. R., Haisch, B. M., and Schmelz, J. T. (eds.), *The Many Faces of the Sun: A Summary of Results from NASA's Solar Maximum Mission*, Springer, New York, p. 143.
Illing, R. M. E., and Hundhausen, A. J.: 1985, *J. Geophys. Res.* **90**, 275–282.
Illing, R. M. E., and Hundhausen, A. J.: 1986, *J. Geophys. Res.* **91**, 10951–10960.
Isenberg, P. A.: 1997, *J. Geophys. Res.* **102**, 4719–4724.
Ivanov, K. G., and Kharshiladze, A. F.: 1985, *Solar Phys.* **98**, 379–386.
Ivanov, K. G., Kharshiladze, A. F., Eroshenko, E. G., and Styazhkin, V. A.: 1989, *Solar Phys.* **120**, 407–419.
Kahler, S. W.: 1994, *Astrophys. J.* **428**, 837–849.
Kennel, C. F., Edmiston, J. P., and Hada, T.: 1985, in: R. G., and Tsurutani, B. T. (eds.), *Collisionless Shocks in the Heliosphere: A Tutorial Review*, Stone, Geophysical Monograph **34**, Amer. Geophys. Union, Washington, DC, pp. 1–36.
Klassen, A., Aurass, H., Klein, K.-L., Hofmann, A., and Mann, G.: 1998, *Astron. Astrophys.* **343**, 287–296.
Klassen, A., Aurass, H., Mann, G., and Thompson, B. J.: 2000, *Astron Astrophys. Suppl.* **141**, 357–369.
Klein, K.-L., Khan, J. I., Vilmer, N., Delouis, J.-M., and Aurass, H.: 1999, *Astron. Astrophys.* **346**, L53–L57.
Klein, K.-L., and Trottet, G.: 2001, *Space Sci. Rev.* **95**, 215–225.
Klein, L. W., and Burlaga, L. F.: 1982, *J. Geophys. Res.* **87**, 613–624.
Klecker, B., Kunow, H., *et al.*: 2006, *Space Sci. Revs.*, this volume.
Kliem, B., Titov, V., and Török, T.: 2004, *Astron. Astrophys.* **413**, L23–L26.
Klimchuk, J. A.: 2001, in: Song, P., Siscoe, G., and Singer, H. (eds.), *Space Weather* (Geophysical Monograph 125), Amer. Geophys. Union, Washington, D.C., pp. 143–157.
Kocharov, L., Vainio, R., Kovaltsov, G. A., and Torsti, J.: 1998, *Solar Phys.* **182**, 195–215.
Kosovichev, A. G., and Zharkova, V. V.: 2001, *Astrophys. J.* **550**, L105–L108.
Kóta, J., and Jokipii, J. R.: 1997, *Proc. 25th Internat. Cosmic Ray Conf. (Durban)* **1**, 213–216.
Koutchmy, S.: 1994, *Adv. Space Res.* **14**(4), 29–39.
Krall, J., Chen, J., and Santoro, R.: 2000, *Astrophys. J.* **539**, 964–982.
Krall, J., Chen, J., Duffin, R. T., Howard, R. A., and Thompson, B. J.: 2000, *Astrophys. J.* **562**, 1045–1057.
Kumar, A., and Rust, D. M.: 1996, *J. Geophys. Res.* **101**, 15667–15684.
Kuperus, M., Raadu, M. A.: 1974, *Astron. Astrophys.* **31**, 189–193.
Kusano, K., Maeshiro, T., Yokoyama, T., and Sakurai, T.: 2004, *Astrophys. J.* **610**, 537–549.
Le Méhauté, B.: 1976, *An Introduction to Hydrodynamics and Water Waves*, Springer-Verlag, New York.

Leblanc, Y., Dulk, G. A., and Bougeret, J.-L.: 1998, *Solar Phys.* **183**, 165–176.
Lee, M. A., and Ryan, J.: 1986, *Astrophys. J.* **303**, 829–842.
Lee, M. A.: 1982, *J. Geophys. Res.* **87**, 5063–5080.
Lee, M. A.: 1983, *J. Geophys. Res.* **88**, 6109–6119.
Lee, M. A.: 2005, *Astrophys. J. Suppl.* **158**, 38–67.
Lepping, R. P., Burlaga, L. F., and Jones, J. A.: 1990, *J. Geophys. Res.* **95**, 11957–11965.
Lepping, R. P., Berdichevsky, D. B., Szabo, A., Arqueros, C., and Lazarus, A. J.: 2003, *Solar Phys.* **212**, 425–444.
Leroy, J. L., Bommier, V., and Sahal-Brechot, S.: 1983, *Solar Phys.* **83**, 135–142.
Leroy, J. L., Bommier, V., and Sahal-Brechot, S.: 1984, *Astron. Astrophys.* **131**, 33–44.
Li, G., Zank, G. P., and Rice, W. K. M.: 2003, *J. Geophys. Res.* **108**, Issue A2 CiteID 1082, DOI 10.1029/2002JA009666.
Lin, J., Forbes, T. G., Isenberg, P. A., and Démoulin, P.: 1998, *Astrophys. J.* **504**, 1006–1019.
Lin, J., Soon, W., and Baliunas, S.: 2003, *New Astron. Revs.*, **47**, 53–84.
Lin, J., Raymond, J. C., and van Ballegooijen, A. A.: 2004, *Astrophys. J.* **602**, 422–435.
Linker, J., and Mikić, Z.: 1995, *Astrophys. J.* **103**, L45–L48.
Linker, J. A., and Mikić, Z.: 1999, in: Crooker, N., Joselyn, J., and Feynman, J. (eds.), *Coronal Mass Ejections*, *Geophys. Monograph*, **99**, Amer. Geophys. Union, Washington, pp. 269–277.
Linker, J. A., Mikić, Z., Biesecker, D. A., Forsyth, R. J., Gibson, S. E., Lazarus, A. J., et al.: 1999, *J. Geophys. Res.* **104**, 9809–9830.
Linker, J. A., Lionello, R., Mikić, Z., and Amari, T.: 2001, *J. Geophys. Res.* **106**, 25165–25176.
Linker, J. A., Mikić, Z., Lionello, R., Riley, P., Amari, T., and Odstrcil, D.: 2003, *Phys. Plasmas* **10**, 1971–1978.
Lionello, R., Mikić, Z., Linker, J. A., and Amari, T.: 2002, *Astrophys. J.* **581**, 718–725.
Lites, B. W., Low, B. C., Martinez Pillet, V., Seagraves, P., Skumanich, A., Frank, Z. A., *et al.*: 1995, *Astrophys. J.* **446**, 877–894.
Litvinenko, Y. E.: 1996, *Astrophys. J.* **462**, 997–1004.
Litvinenko, Y. E., and Martin, S. F.: 1999, *Solar Phys.* **190**, 45–58.
Livi, S. H. B., Wang, J., Martin, S. F.: 1985, *Aust. J. Phys.* **38**, 855–873.
Livi, S. H. B., Martin, S. F., Wang, H., and Guoxiang, A.: 1989, *Solar Phys.* **121**, 197–214.
Low, B. C.: 1981, *Astrophys. J.* **251**, 352–363.
Low, B. C.: 2001, *J. Geophys. Res.* **106**, 25141–25164.
Low, B. C., and Zhang, M.: 2002, *Astrophys. J.* **564**, L53–L56.
Lundquist, S.: 1950, *Ark. Fys.* **2**, 361–365.
Lynch, B., MacNeice, P., Antiochos, S. K., Zurbuchen, T., and Fisk, L.: 2004, *Astrophys. J.* **617**, 589–599.
MacNeice, P. J., Antiochos, S. K., Phillips, A., Spicer, D. S., DeVore, C. R., and Olson, K.: 2004, *Astrophys. J.* **614**, 1028–1041.
Malkov, M. A.: 1998, *Phys. Rev. E* **58**, 4911–4928.
Manchester, W. B., Gombosi, T. I., Roussev, I., Ridley, A., De Zeeuw, D. L., Sokolov, I. V., et al.: 2004, *J. Geophys. Res.* **109** Issue A2 CiteID A02107, DOI 10.1029/2003JA010150.
Mann, G., Lühr, H., and Baumjohann, W.: 1994, *J. Geophys. Res.* **99**, 315–333.
Mann, G., Jansen, F., MacDowall, R. J., Kaiser, M. I., and Stone, R. G.: 1999a, *Astron. Astrophys.* **348**, 614–620.
Mann, G., Aurass, H., Klassen, A., Estel, C., and Thompson, B. J.: 1999b, *Proc. 8th SOHO Workshop* ESA **SP-446**, 477–481.
Mann, G., Klassen, A., Aurass, H., and Classen, H.-T.: 2003, *Astron. Astrophys.* **400**, 329–336.
Manoharan, P. K., and Kundu, M.: 2003, *Astrophys. J.* **592**, 597–606.

Martin, S. F., and Echols, C. R.: 1994, in: Rutten, R. J., and Schrijver, C. J. (eds.), *Solar Surface Magnetism, Proc. NATO Adv. Res. Workshop, Soesterberg, The Netherlands, November 1–5, 1993*, Kluwer Academic Publishers, Dordrecht, pp. 339–346.

Martin, S. F., Livi, S. H. B., Wang, J., and Shi, Z.: 1984, in: Hagyard, M. J. (ed.), *Measurements of Solar Vector Magnetic Fields*, NASA Conf. Pub. 2374, pp. 403–436.

Martin, S. F., Livi, S. H. B., and Wang, J.: 1985, *Australian J. Phys.* **38**, 929–959.

Martin, S. F., Bilimoria, R., and Tracadas, P. W.: 1994, in: Rutten, R. J., and Schrijver, C. J. (eds.), *Solar Surface Magnetism, Proc. NATO Adv. Res. Workshop, Soesterberg, The Netherlands, November 1–5, 1993*, Kluwer Academic Publishers, Dordrecht, p. 303–338.

Marubashi, K.: 1997, *Coronal Mass Ejections. Geophys. Monograph 99*, Crooker, N., Joselyn, J. A., and Feynman, J. (eds.), Amer. Geophys. Union, Washington, DC, pp. 147–156.

McComas, D. J., Gosling, J. T., Hammond, C. M., Moldwin, M. B., Philips, J. L., and Forsyth, R. J.: 1994, *Geophys. Res. Lett.* **21**, 1751–1754.

Mikić, Z., Barnes, D., and Schnack, D.: 1988, *Astrophys. J.* **328**, 830–847.

Mikić, Z., and Lee, M. A.: 2006, *Space Sci. Revs.*, this volume.

Moldwin, M. B., Phillips, J. L., Gosling, J. T., Scime, E. E., McComas, D. J., Bame, S., et al.: 1995, *J. Geophys. Res.* **100**, 19903–19910.

Moore, R. L., and Roumeliotis, G.: 1992, in: Švestka, Z., Jackson, B., and Machado, M. (eds.), *Eruptive Solar Flares. Proc. IAU Colloquium 133, Iguazu, Argentina, August 2–6, 1991*, New York, Springer-Verlag, pp. 69–78.

Mulligan, T., and Russell, C. T.: 2001, *J. Geophys. Res.* **106**, 10581–10596.

Newkirk, G. A.: 1961, *Astrophys. J.* **133**, 983–994.

Odstrcil, D., and Pizzo, V. J.: 1999a, *J. Geophys. Res.* **104**, 483–492.

Odstrcil, D., and Pizzo, V. J.: 1999b, *J. Geophys. Res.* **104**, 493–504.

Odstrcil, D., and Pizzo, V. J.: 1999c, *J. Geophys. Res.* **104**, 28225–28239.

Odstrcil, D., Linker, J., Lionello, R., Mikić, Z., Riley, P., Pizzo, V., *et al.*: 2002, *J. Geophys. Res.* **107**, Issue A12 CiteID 1493, DOI 10.1029/2002JA009334.

Osherovich, V. A., Farrugia, C. J., Burlaga, L. F., Lepping, R. P., Fainberg, J., and Stone, R. G.: 1993, *J. Geophys. Res.* **98**, 15331–15342.

Owens, M. J., Crooker, N. U., Siscoe, G., Pagle, C., and Cargill, P. J.: 2005, *J. Geophys. Res.* **110**, Issue A1 CiteID A01105 10.1029/2004JA010814.

Palmer, I. D.: 1982, *Rev. Geophys. Space Phys.* **20**, 335–351.

Parker, E. N.: 1958, *Astrophys. J.* **128**, 664–672.

Pick, M., Forbes, T. G., Mann, G., *et al.*: 2006, *Space Sci. Revs.*, this volume.

Priest, E. R.: 1982, *Solar Magnetohydrodynamics*, Reidel, Dordrecht.

Reames, D. V., Barbier, L. M., and Ng, C. K.: 1996, *Astrophys. J.* **466**, 473–486.

Reiner, M. J., Kaiser, M. L., and Bougeret, J.-L.: 2003, in: Velli, M. *et al.* (eds.), *Solar Wind Ten*, Amer. Inst. Phys., New York, pp. 152–155.

Rice, W. K. M., Zank, G. P., and Li, G.: 2003, *J. Geophys. Res.* **108** Issue A10 CiteID 1369 DOI 10.1029/2002JA009756.

Richardson, I. G., Cane, H. V.: 2004, *Geophys. Res. Lett.* **31** Issue 18 CiteID L18804 DOI 10.1029/2004GL020958.

Riley, P., and Crooker, N. U.: 2004, *Astrophys. J.* **600**, 1035–1042.

Riley, P., Gosling, J. T., and Pizzo, V. J.: 1997, *J. Geophys. Res.* **102**, 14677–14686.

Riley, P., Linker, J. A., Mikić, Z., Odstrcil, D., Zurbuchen, T., Lario, D., *et al.*: 2003, *J. Geophys. Res.* **108** Issue A7 CiteID 1272 DOI 10.1029/2002JA009760.

Riley, P., Linker, J. A., Lionello, R., Mikic, Z., Odstrcil, D., Hidalgo, M. A., et al.: 2004, . *Atmos. Solar-Terr. Phys.* **66**, 1321–1331.

Rogers, B. N., Drake, J. F., and Shay, M. A.: 2000, *Geophys. Res. Lett.* **27**, 3157–3160.

Romashets, E. P., and Ivanov, K. G.: 1991, *Geomag. Aeron.* **31**, 583–586.

Roussev, I. I., Forbes, T. G., Gombosi, T., Sokolov, I. V., De Zeeuw, D., and Birn, J.: 2003, *Astrophys. J.* **588**, L45–L48.
Roussev, I. I., Sokolov, I. V., Forbes, T. G., Gombosi, T. I., Lee, M. A., and Sakai, J. I.: 2004, *Astrophys. J.* **605**, L73–L76.
Ruffolo, D.: 1995, *Astrophys. J.* **442**, 861–874.
Russell, C. T., and Mulligan, T.: 2002, *Adv. Sp. Res.* **29**, 301–306.
Rust, D. M., and Kumar, A.: 1994, *Solar Phys.* **155**, 69–97.
Schmidt, J. M., and Cargill, P. J.: 2001, *J. Geophys. Res.* **106**, 8283–8290.
Schmidt, J. M., and Cargill, P. J.: 2003, *J. Geophys. Res.* **108**, Issue A1 CiteID 1023, DOI 10.1029/2002JA009325.
Schmidt, J. M., and Cargill, P. J.: 2004, *Annales Geophys.* **22**, 2245–2254.
Schmidt, J. M.: 2000, *Solar Phys.* **197**, 135–148.
Scholer, M., Kucharek, H., and Giacalone, J.: 2000, *J. Geophys. Res.* **105**, 18285–18294.
Schwartz, S. J., Burgess, D., Williamson, W. P., Kessel, R. L., Dunlop, M., and Lühr, H.: 1992, *J. Geophys. Res.* **97**, 4209–4227.
Shafranov, V.D.: 1966, *Revs. of Plasma Phys.* **2**, 103–151.
Sheeley, Jr., N. R., Walters, J. H., Wang, Y.-M., and Howard, R. A.: 1999, *J. Geophys. Res.* **104**, 24739–24767.
Schwenn, R., Raymond, J. C., *et al.*: 2006, *Space Sci. Revs.*, this volume.
Srivastava, N., Schwenn, R., Inhester, B., Martin, S. F., and Hanaoka, Y., *Astrophys. J.* **534**, 468–481.
Skilling, J.: 1971, *Astrophys. J.* **170**, 265–273.
Sokolov, I. V., Roussev, I. I., Gombosi, T. I., Lee, M. A., Kóta, J., Forbes, T. G., *et al.*: 2004, *Astrophys. J.* **616**, L171–L174.
Somov, B. V., Kosugi, T., Hudson, H. S., Sakao, T., Masuda, S.: 2002, *Astrophys. J.* **579**, 863–873.
Steinolfson, R. S., and Nakagawa, Y.: 1977, *Astrophys. J.* **215**, 345–355.
Sterling, A. C., and Moore, R. L.: 2001, *J. Geophys. Res.* **106**, 25227–25238.
Sterling, A. C., and Moore, R. L.: 2004, *Astrophys. J.* **602**, 1024–1036.
Sterling, A. C., Moore, R. L., Qiu, J., and Wang, H.: 2001, *Astrophys. J.* **561**, 1116–1126.
Sturrock, P.: 1991, *Astrophys. J.* **380**, 655–659.
Sturrock, P. A., Weber, M., Wheatland, M. S., and Wolfson, R.: 2001, *Astrophys. J.* **548**, 492–496.
Subramanian, P., Ananthakrishnan, S., Janardhan, P., Kundu, M. R., White, S. M., and Garaimov, V. I.: 2003, *Solar Phys.* **218**, 247–259.
Suess, S. T.: 1988, *J. Geophys. Res.* **93**, 5437–5445.
Švestka, Z., and Cliver, E.: 1992, in: Švestka, Z., Jackson, B., and Machado, M. (eds.), *Eruptive Solar Flares*, New York: Springer-Verlag, pp. 1–14.
Titov, V., and Démoulin, P.: 1999, *Astron. Astrophys.* **351**, 701–720.
Tokman, M., and Bellan, P.: 2002, *Astrophys. J.* **567**, 1202–1210.
Tsuneta, S., and Naito, T.: 1998, *Astrophys. J.* **495**, L67–L70.
Tylka, A. J., Cohen, C. M. S., Dietrich, W. F., Lee, M. A., Maclennan, C. G., Mewaldt, R. A., *et al.*: 2005, *Astrophys. J.* **625**, 474–495.
Vainio, R., and Khan, J. I.: 2004, *Astrophys. J.* **600**, 451–457.
Vandas, M., Fischer, S., and Geranios, A.: 1991, *Planet. Space Sci.* **39**, 1147–1154.
Vandas, M., Fischer, S., Pelant, P., and Geranios, A.: 1992, in: Marsch, E., and Schwenn, R. (eds.), *Solar Wind Seven*, *Pergamon*, New York, pp. 671–674.
Vandas, M., Fischer, S., Pelant, P., and Geranios, A.: 1993, *J. Geophys. Res.*, **98** 11467–11475.
Vainio, R., and Schlickeiser, R.: 1999, *Astron. Astrophys.* **343**, 303–311.
Vainio, R., Kocharov, L., and Laitinen, T.: 2000, *Astrophys. J.* **528**, 1015–1025.
Vainio, R.: 1997, *Proc. 25th Internat. Cosmic Ray Conf. (Durban)* **1**, 253–256.

Vainio, R.: 1999, in: Ostrowski, M., and Schlickeiser, R. (eds.), *Plasma Turbulence and Energetic Particles in Astrophysics*, Obserwatorium Astronomiczne, Uniwersytet Jagielloński), Cracow, pp. 232–245.
Vainio, R.: 2003, *Astron. Astrophys.* **406**, 735–740.
van Ballegooijen, A. A.: 2004, *Astrophys. J.* **612**, 519–529.
van Ballegooijen, A.A., and Martens, P. C. H.: 1989, *Astrophys. J.* **343**, 971–984.
van der Linden, R. A. M., Hood, A. W., and Goedbloed, J. P.: 1994, *Solar Phys.* **154**, 69–96.
van Nes, P., Reinhard, R., Sanderson, T. R., Wenzel, K.-P., and Zwickl, R. D.: 1984, *J. Geophys. Res.* **89**, 2122–2132.
van Tend, W., and Kuperus, M.: 1978, *Solar Phys.* **59**, 115–127.
Vandas, M., Fischer, S., Dryer, M., Smith, Z., and Detman, T.: 1995, *J. Geophys. Res.* **100**, 12285–12292.
Vandas, M., Fischer, S., Dryer, M., Smith, Z., and Detman, T.: 1996, *J. Geophys. Res.* **101**, 2505–2510.
Wagner, W., Hildner, E., House, L., Sawyer, C., Sheridan, K., and Dulk, G.: 1981, *Astrophys. J.* **244**, L123–L126.
Wang, H., Qiu, J., Jing, J., and Zhang, H.: 2003, *Astrophys. J.* **593**, 564–570.
Wang, Y.-M.: 2001, *Astrophys. J.* **560**, 456–465.
Wang, Y.-M., Nash, A. G., and Sheeley, Jr. N. R.: 1989, *Science* **245**, 712–718.
Wang, Y.-M., and Sheeley Jr., N. R.: 1990, *Astrophys. J.* **365**, 372–386.
Welsch, B. T., Abbett, W. P., Fisher, G. H., and Regnier, S.: 2004, *Astrophys. J.* **610**, 1148–1156.
Wimmer-Schweingruber, R. F., Crooker, N. U., *et al.*: 2006, *Space Sci. Revs.*, this volume.
Wood, B. E., Karovska, M., Chen, J., Brueckner, G. E., Cook, J. W., and Howard, R. A.: 1999, *Astrophys. J.* **512**, 484–495.
Wu, C. S.: 1984, *J. Geophys. Res.* **89**, 8857–8862.
Wu, S. T., Guo, W. P., and Wang, J. F.: 1995, *Solar Phys.* **157**, 325–248.
Wu, S. T., Guo, W. P., and Dryer, M.: 1997, *Solar Phys.* **170**, 265–282.
Wu, S. T., Guo, W. P., Michels, D. J., and Burlaga, L. F.: 1999, *J. Geophys. Res.* **104**, 14789–14802.
Wu, S. T., Andrews, M. D., and Plunkett, S. P.: 2001, *Space Sci. Revs.* **95**, 191–213.
Zalesak, S. T.: 1979, *J. Comput. Phys.* **3** 335–362.
Zank, G. P., Rice, W. K. M., and Wu, C. C.: 2000, *J. Geophys. Res.* **105**, 25079–25096.
Zhang, J.: 2005, in: Dere, K., Wang, J., and Yan, Y. (eds.), *Coronal and Stellar Mass Ejections, Proc. IAU Symp. 226*, Cambridge Univ. Press., Cambridge, UK, pp. 65–70.
Zhang, J., Dere, K., Howard, R., and Vourlidas, A.: 2004, *Astrophys. J.* **604**, 420–432.